

Rat Organic Cation Transporter 1 Contains Three Binding Sites for Substrate 1-Methyl-4-phenylpyridinium per Monomer

**Thorsten Keller, Valentin Gorboulev, Thomas D. Mueller, Volker
Dötsch, Frank Bernhard, and Hermann Koepsell**

*Institute of Anatomy and Cell Biology, University of Würzburg, 97070 Würzburg,
Germany (T.K., V.G., H.K.); Department of Molecular Plant Physiology and
Biophysics, Julius-von-Sachs-Institute, University of Würzburg, 97082 Würzburg,
Germany (T.K., T.D.M., H.K.); Department of Biophysical Chemistry, University of
Frankfurt, 60439 Frankfurt am Main, Germany (V.D., F.B.)*

Running title: OCT1 Contains Three Substrate Binding Sites per Monomer

Address correspondence to: Hermann Koepsell, Department of Molecular Plant Physiology and Biophysics, Julius-von-Sachs-Institute, Julius-von-Sachs-Platz 2, 97082 Würzburg, Germany, phone +49 931 3182700; fax +49 931 3182087; E-mail: Hermann@Koepsell.de

Number of text pages: 25

Number of tables: 2

Number of figures: 9

Number of references: 47

Number of words in the abstract: 245

Number of words in the introduction: 737

Number of words in the discussion: 1495

ABBREVIATIONS: B_{\max} , maximal binding; CHAPS, 3-[(3-cholamidopropyl)dimethylammonio]-1-propanesulfonate; EMA, European Medicine Agencies; DMPG, 1,2-dimyristoyl-*sn*-[phospho-*rac*-(1-glycerol)]; DPPC, 1,2-dipalmitoyl-*sn*-glycero-3-phosphocholine; EC₅₀, half maximal effective concentration; FDA, American Food and Drug Administration; GFP, green fluorescent protein; HEK, human embryonic kidney; ND, nanodisc; OCT, organic cation transporter; rOCT, rat organic cation transporter; hOCT, human organic cation transporter; MFS, major facilitator superfamily; MPP⁺, 1-methyl-4-phenylpyridinium⁺; MSP, major scaffold protein; Ni²⁺-NTA, Ni²⁺-nitriloacetic acid; NME, novel molecular entity; PC, phosphatidylcholine; PCR, polymerase chain reaction; POPC, 1-palmitoyl-2-oleoyl-*sn*-glycero-3-phosphocholine; PS, phosphatidylserine; SDS-PAGE, SDS-polyacrylamide gel electrophoresis; TBuA⁺, tetrabutylammonium⁺; 3D, three-dimensional

ABSTRACT

Organic cation transporters OCT1 (*SLC22A1*) and OCT2 (*SLC22A2*) are critically involved in absorption and excretion of diverse cationic drugs. Because drug-drug interactions at these transporters may induce adverse drug effects in patients, *in vitro* testing for interaction with the human transporters during drug development is mandatory. Recent data performed with rat OCT1 (rOCT1) suggest that currently performed *in vitro* tests assuming one polyspecific binding site are insufficient. Here we measured binding and transport of model substrate 1-methyl-4-phenylpyridinium⁺ (MPP⁺) by cell-free-expressed fusion proteins of rOCT1 and various rOCT1 mutants with green fluorescent protein that were reconstituted into nanodiscs or proteoliposomes. The nanodiscs were formed with major scaffold protein MSP and different phospholipids whereas the proteoliposomes were formed with a mixture of cholesterol, phosphatidylserine and phosphatidylcholine. In nanodiscs formed with 1-palmitoyl-2-oleoyl-*sn*-glycero-3-phosphocholine or cholesterol, phosphatidylserine and phosphatidylcholine two low-affinity MPP⁺ binding sites and one high-affinity MPP⁺ binding site per transporter monomer were determined. Mutagenesis revealed that tryptophan 218 and aspartate 475 in neighboring positions in the modeled outward-open cleft contribute to one low-affinity binding site whereas arginine 440 located distantly in the cleft is critical for MPP⁺ binding to another low-affinity site. Comparing MPP⁺ binding with MPP⁺ transport suggests that the low-affinity sites are involved in MPP⁺ transport whereas high-affinity MPP⁺ binding influences transport allosterically. The data provide a rationale for future reliable, more sophisticated *in vitro* testing and for the generation of pharmacophore models with high predictive power. They will be helpful to interpret future crystal structures.

Introduction

The polyspecific organic cation transporters OCT1 (*SLC22A1*), OCT2 (*SLC22A2*) and OCT3 (*SLC22A3*) play a pivotal role in absorption, tissue distribution and elimination of cationic drugs including psychopharmaca, cytostatics, antidiabetics and antiviral drugs (Koepsell et al., 2007; Nies et al., 2010; Minuesa et al., 2011; Amphoux et al., 2006). These transporters also have important physiological functions because they translocate various endogeneous cations. To anticipate drug-drug interactions at the level of individual organic cation transporters (OCTs) *in vitro* evaluation of novel drugs for interaction with human OCT1 (hOCT1) and OCT2 (hOCT2) has been recommended (Giacomini et al., 2010, Zamek-Gliszczynski et al., 2018) and is demanded by the American Food and Drug Administration (FDA, 2017) and the European Medicine Agencies (EMA, 2012). Currently novel molecular entities (NMEs) are tested for interaction with hOCT1 and hOCT2 expressed in epithelial cells analyzing whether they inhibit uptake of a cationic model substrate that is applied at a micromolar concentration (Ahlin et al., 2008; Ahlin et al., 2011; Chen et al., 2017). This procedure turned out to be insufficient because it was observed that the efficacy of inhibitors was dependent on the molecular structure of the employed substrate and was different when substrate concentrations far below their respective Michelis-Menten constant (K_m) values were used for uptake measurements (Thevenod et al., 2013; Belzer et al., 2013; Minuesa et al., 2017; Yin et al., 2016; Gorboulev et al., 2018; Sandoval et al. 2018). For example, high affinity inhibition of uptake of 1-methyl-4-phenylpyridinium⁺ (MPP⁺) by hOCT1, hOCT2 and human OCT3 (hOCT3) by the nucleoside reverse transcriptase inhibitor tenofovir disoproxil fumarate was observed when uptake was measured with 12.5 nM MPP⁺, but did not show up when uptake was performed with 1 μ M MPP⁺ (Minuesa et al.,

2009; Minuesa et al., 2017). These observations indicate the necessity of more sophisticated *in vitro* testing of NMEs during drug development (Koepsell 2018). To establish appropriate test protocols and to enforce their application by pharmaceutical companies, a basic experimentally supported concept how different drugs can interact at individual OCTs is imperatively needed.

The current knowledge about function and substrate recognition by OCTs is mainly based on studies performed with rat OCT1 (rOCT1) and rat OCT2 (rOCT2). Evidence has been provided that rOCT1 and rOCT2 are facilitated diffusion systems that may operate as electrogenic cation uniporters or electroneutral cation exchangers (Busch et al., 1996; Budiman et al., 2000; Keller et al., 2005; Schmitt and Koepsell, 2005). The apparent K_m values of OCTs for different substrates are in the micromolar and millimolar concentration range. In addition, high-affinity cation interaction sites with half maximal effective concentrations (EC_{50}) in the picomolar and nanomolar range have been determined that may be inhibitory (Gorbunov et al., 2008; Minuesa et al., 2009). Homo-oligomerisation of OCT1 and OCT2 has been demonstrated (Keller et al., 2011; Brast et al., 2012), however, it remained unclear whether high-affinity binding is dependent on oligomerization. To obtain molecular insight into polyspecific binding and transport extensive mutagenesis was performed in rOCT1. Effects on apparent K_m values and on half maximal concentrations (IC_{50}) values of inhibitors were interpreted with the help of homology models derived from crystal structures of bacterial transporters of the same major facilitator superfamily (MFS) (Gorboulev et al., 2005; Popp et al., 2005; Volk et al., 2009; Gorboulev et al., 2018; Gorboulev et al., 1999; Egenberger et al., 2012). The data support the hypothesis that rOCT1 contains clefts with cation binding domains in the outward- or inward-open conformation, which contain overlapping binding sites for structurally

different cations. However, these interpretations remained speculative because changes in K_m and IC_{50} values observed upon mutagenesis do not directly reflect effects on binding of substrates and/or inhibitors.

In the present study we measured binding of radioactively labeled 1-methyl-4-phenylpyridinium⁺ (MPP⁺) to cell-free-expressed fusion proteins of rOCT1 and various rOCT1 mutants with green fluorescent protein (GFP) that were reconstituted into nanodiscs (NDs). We analysed apparent dissociation constant (K_D) values for MPP⁺ binding to reconstituted NDs and the amounts of MPP⁺ per rOCT1 monomer in the preparation. In addition, we reconstituted the proteins into proteoliposomes and determined the effects of the mutations on the apparent K_m values and the turnover numbers. We observed that each rOCT1 monomer contained two low-affinity MPP⁺ binding sites that are directly engaged in transport and one high-affinity MPP⁺ binding site that exhibits allosteric effects on the low-affinity sites. These data provide a basis to understand interactions of cationic ligands at the highly polyspecific organic cation transporters.

Materials and Methods

Materials. [³H]-1-methyl-4-phenylpyridinium⁺ (MPP⁺) (3.1 TBq/mmol) was obtained from ART Chemicals (Amsterdam, Holland). 1-myristoyl-2-hydroxy-*sn*-glycero-3(phospho-*rac*-(1-glycerol)) (cat# 858120), 1,2-dimyristoyl-*sn*-glycero-3-phospho-(1-*rac*-glycerol) (DMPG) (cat# 840445P), 1,2-dipalmitoyl-*sn*-glycero-3-phosphocholine (DPPC) (cat# 850355P) and 1-palmitoyl-2-oleoyl-*sn*-glycero-3-phosphocholine (POPC) (cat# 850457P) were purchased from Avanti Polar Lipids (Alabaster, AL). Cholesterol (cat# C8667), 1,2-diacyl-*sn*-glycero-3-phosphocholine from egg yolk (PC)

(cat# P3556), 1,2-diacyl-*sn*-glycero-3-phospho-L-serine from bovine brain (PS) (cat# P7769), and goat anti-rabbit IgG antibody coupled to horse radish peroxidase (cat#12-348) were delivered by Sigma-Aldrich (Schnelldorf, Germany). Dodecylphosphocholine (cat# F308S) was obtained from Anatrace (Maumee, OH) and 3-[(3-cholamidopropyl)dimethylammonio]-1-propanesulfonate (CHAPS) (cat# A1099) from AppliChem GmbH (Darmstadt, Germany). *E. coli* strain BL21 Star(D3) (cat# C6010-03) was purchased from Invitrogen Thermo Fischer Scientific (Carlsbad, CA) and *E. coli* strain A19 (cat#5997) from Coli Genetic Stock Center (New Haven CT). Plasmid EGFP-C1 (cat# 6084-1) was obtained from Takara Bio USA, plasmid pIVEX2.3 MCS (cat# 3 253 538) from Roche Diagnostics (Mannheim, Germany), plasmid pET21a (cat# 69740-3) from Merck Life Science GmbH (Eppelheim, Germany), and plasmid pcDNA3.1 (Cat# V790-20) from Invitrogen Thermo Fischer Scientific. Other materials were obtained as described (Keller et al., 2008).

Cloning. For cloning of the fusion proteins, the GFP mutant A206K was employed which does not form dimers (Zacharias et al., 2002). The GFP(A206K) mutant was created by polymerase chain reaction (PCR) using EGFP-C1 plasmid as template. A forward flanking primer with the NdeI recognition site and a reverse flanking primer with the BamHI recognition sequence followed by an XhoI site were employed. The amplificate was cut with NdeI/XhoI and cloned into the respective sites of the pIVEX2.3 MCS vector.

To generate GFP(A206K)-rOCT1, GFP(A206K) cDNA was cloned upstream of rOCT1 into NdeI/BamHI sites of the rOCT1-His/pET21a plasmid (Keller et al., 2011). The resulting plasmid was cut with NdeI/XhoI and GFP(A206K)-rOCT1WT cDNA was transferred into the NdeI/XhoI sites of the vector pIVEX2.3 MCS coding GFP(A206K)-rOCT1 protein with a His-tag at the C-terminus.

Mutants GFP(A206K)-rOCT1(F160Y), GFP(A206K)-rOCT1(W218L) and GFP(A206K)-rOCT1(W218Y) were cloned by replacing the Eco147I/Eco81I fragment of the rOCT1 by the fragments of the respective rOCT1 mutants prepared previously (Popp et al., 2005; Volk et al., 2009).

Mutants GFP(A206K)-rOCT1(R440K), GFP(A206K)-rOCT1(L447Y), GFP(A206K)-rOCT1(L447F), GFP(A206K)-rOCT1(Q448E) and GFP(A206K)-rOCT1(D475E) were generated by replacing the Eco81I/XhoI fragment of the rOCT1 by the respective fragments of rOCT1 mutants described earlier (Volk et al., 2009; Gorboulev et al., 2005; Gorboulev et al., 1999). To construct the rOCT1 double mutant GFP(A206K)-rOCT1(W218Y/D475E), the Eco81I/XhoI fragment of GFP(A206K)-rOCT1(W218Y) was replaced by the respective fragment of the GFP(A206K)-rOCT1(D475E). The rOCT1 double mutant GFP(A206K)-rOCT1(R440K/D475E) was made by PCR using the GFP(A206K)-rOCT1(D475E) as a template.

For cloning of GFP(A206K)-rOCT1(6 Δ C) the pIVEX2.3 MCS vector was used after removal of the unique BamHI site. Therefor the plasmid was linearized with BamHI, the ends were filled using DNA polymerase I, and the plasmid was ligated. The GFP(A206K)-rOCT1 cDNA was cloned first into the NdeI/XhoI sites of this vector. Then the BamHI/Eco81I fragment of the rOCT1 WT was replaced by the respective fragment of the rOCT1(6 Δ C) which was prepared from the previously described GFP-rOCT1(6 Δ C)/pcDNA3.1 plasmid (Keller et al., 2011).

Expression and purification of MSP1E3D1. A His-tagged elongated construct of membrane scaffold protein 1 which contains a truncated first α -helix (MSP1E3D1) (Denisov et al., 2004; Roos et al., 2012) was expressed in *E. coli*. Bacteria (*E. coli* strain BL21(DE3)Star) were transformed with pET28a plasmid encoding His-tagged MSP1E3D1 and grown to mid-log phase. Protein expression was induced by

isopropyl- β -D-thiogalactopyranosid and bacteria were grown for 3 h at 30°C. After 15 min centrifugation at 6,000 \times g, bacteria were washed, suspended in 20 mM Tris-HCl pH 8.0 containing 500 mM NaCl and 50 mM imidazole, lysed by sonication at 4°C, and cellular debris was removed by 1 h centrifugation at 100,000 \times g. For protein purification the supernatant was mixed with Ni²⁺-nitriloacetic acid (Ni²⁺-NTA)-agarose, incubated for 1 h under rotation, and poured into an empty gravity flow column. After extensive washing with 20 mM Tris-HCl, pH 8.0 containing 500 mM NaCl and 50 mM imidazole, protein was eluted with the same buffer containing 500 mM imidazole. Fractions containing purified protein were pooled. Aliquots were snap frozen in liquid nitrogen and stored at -80°C.

Formation of empty nanodiscs. 0.1% (w/v) dodecyl-phosphocholine containing 20 μ M MSP1E3D1 plus either 2.2 mM 1,1-dimyristoyl-*sn*-[phospho-*rac*-(1-glycerol)] (DMPG) or 2.2 mM 1,1-dipalmitoyl-*sn*-glycero-3-phosphocholine (DPPC) or 2.2 mM 1-palmitoyl-2-oleoyl-*sn*-glycero-3-phosphocholine (POPC) or 0.6 mg/ml cholesterol, 0.2 mg/ml phosphatidylcholine (PC) and 1 mg/ml phosphatidylserine (PS) were incubated for 1 h at room temperature. For nanodisc (ND) formation the mixture was dialysed for 48 h at 0°C against excess of dialysis buffer (40 mM Tris-HCl, pH 8.0, 100 mM NaCl) employing three buffer changes. Residual aggregates were separated from soluble NDs by 20 min centrifugation at 22,000 \times g. The supernatant was transferred to Centriprep concentrator devices (10 kDa MWCO, Millipore, Merck, Darmstadt, Germany). After equilibration with 3 ml dialysis buffer the concentrator devices were centrifuged at 2,000 \times g (4 °C) and NDs were concentrated up to final MSP1E3D1 concentrations of 2.4 mM corresponding to a concentration of NDs of 1.2 mM. After another 20 min centrifugation at 22,000 \times g the NDs in the supernatant were

kept on ice before usage. For long time storage, NDs were snap frozen in liquid nitrogen and stored at -80°C .

Cell-free expression and insertion into nanodiscs. Extracts for cell-free expression were isolated from *E. coli* strain A19 and reaction mixtures containing vectors and cell-free extracts as well as feeding mixtures were prepared as described (Klammt et al., 2004). Cell-free expression of GFP-rOCT1 wildtype and mutants and cotranslational insertion into nanodiscs was performed in the absence of detergent in the continuous exchange mode. Dispodialysers from Spectrum Laboratories Inc. (Breda, Netherlands) with a cutoff of 25 kDa and a 1-ml reaction volume were used. For co-translational membrane insertion of the transport proteins during cell-free synthesis, 150 μM of empty NDs were added to the reaction mixtures. Cell-free reaction was performed by shaking the Dispodialysers filled with reaction mixtures for 20 h at 30°C in glass tubes containing 17 ml feeding mixture. Thereafter the reaction mixture was centrifuged for 10 min at $10,000\times g$ (4°C) and the supernatant containing empty NDs and the NDs with reconstituted transport proteins was harvested. For binding measurements Ni^{2+} -NTA-agarose beads were added to the supernatant and the beads with attached NDs were precipitated.

Measurement of MPP⁺-binding. NDs attached to Ni^{2+} -NTA-agarose beads were incubated for 1 min at 37°C or 0°C with phosphate buffered saline, pH 7.4 (PBS) containing 12.5 nM MPP⁺ traced with [^3H]MPP⁺ without and with different additional concentrations of nonradioactive MPP⁺. The samples were washed for about 10 s with 5 ml of ice-cold PBS on 0.22 μm cellulose acetate filters. The filters were dissolved in LUMASAFETM PLUS mixture (Lumac LSC, Groningen, The Netherlands) and assayed for radioactivity by liquid scintillation counting. One min incubation with MPP⁺ at 37°C was shown to be long enough to achieve saturation of binding at high-

and low-affinity MPP⁺ binding sites of GFP-rOCT1 (Supplemental Fig. 1, left panel). Since MPP⁺ binding to GFP-rOCT1 was not decreased when washing of the filters was extended using 10 ml or 15 ml of washing buffer, a dissociation of bound MPP⁺ during routine washing with 5 ml is considered negligible (Supplemental Fig. 1, right panel). Because the slow dissociation of MPP⁺ can be due to a structural change of the transporter that may be induced by MPP⁺ binding and/or by cooling during the washing procedure, the determined dissociation constants are considered as apparent dissociation constants.

Purification of cell-free expressed transporters. Cell-free expression was performed in the absence of detergent without addition of NDs as described above. The pellet obtained after 10-min centrifugation at 10,000×g (4°C) was washed with Tris buffer (20 mM Tris-HCl, pH 8, 500 mM NaCl) containing 10 mM imidazole. The precipitate was solubilized by 1-hour incubation at 30°C with 1 ml of 2% (w/v) 1-myristoyl-2-hydroxy-*sn*-glycero-3(phospho-*rac*-(1-glycerol)) dissolved in Tris buffer containing 10 mM imidazole and centrifuged for 10 min at 10,000×g (4°C). The supernatant was mixed with 11 ml of Tris buffer containing 10 mM imidazole plus 1% (w/v) CHAPS and Ni²⁺-NTA-agarose and incubated for 1 hour at 4°C. The suspension was poured into a column and washed with Tris buffer containing 1% CHAPS and 10 mM imidazole and Tris buffer containing 1% CHAPS and 20 mM imidazole. Proteins were eluted with 5 ml of Tris buffer containing 1% CHAPS and 100 mM imidazole.

Reconstitution of proteoliposomes. For freeze-thaw reconstitution protein-lipid aggregates were mixed with large multilamellar liposomes, and the mixture was frozen, thawed, pelleted and homogenized as described (Keller et al., 2011). Protein-lipid aggregates were formed as follows: Cholesterol, PC and PS (1 mg each) were

dissolved in 1 ml chloroform/methanol (1:1, v/v), dried in a round bottom flask under nitrogen, and 500 μ l of the purified protein solved in CHAPS was added. The mixture was shaken for 1 h at 4°C, and CHAPS was removed by dialysis at 4°C against 20 mM Tris/HCl, 500 mM NaCl, and 100 mM choline chloride. After 30-min centrifugation at 200,000 \times g (4°C) the sediment was suspended in 2 ml ice-cold KC buffer (20 mM imidazole, pH 7.4, 0.1 mM Mg²⁺, 100 mM K⁺, 100 mM cyclamate⁻), again centrifuged at 200,000 \times g, and the pellet was suspended in 150 μ l of KC buffer. Large multilamellar liposomes were prepared in the following way: 2 mg of cholesterol and 4 mg of PS in 1 ml of chloroform/methanol (1:1, v/v) were dried in a round bottom flask under nitrogen, 1 ml of KC buffer was added, and the flask was shaken for 3 h at room temperature. Aggregates were removed by 10-min centrifugation at 10,000 \times g. The multilamellar liposomes in the supernatant were pelleted by 15-min centrifugation at 200,000 \times g and suspended in 150 μ l of KC buffer (room temperature). For the formation of large proteoliposomes 150 μ l of the protein-lipid aggregates were mixed with 150 μ l of the multilamellar liposomes, incubated for 15 min at 41°C and frozen in liquid nitrogen. Before transport measurements were started the sample was thawed at 37°C in a water bath, 1.7 ml KC buffer (room temperature) was added, the proteoliposomes were pelleted by 15-min centrifugation at room temperature, the pellet was resuspended in 300 μ l KC buffer (room temperature) and homogenized by repeated suction into and forced extrusion out of a 100- μ l pipette tip.

Measurement of MPP⁺-uptake into proteoliposomes. The proteoliposomes were preincubated for 10 min at 37°C with 20 μ M valinomycin in the absence or presence of 100 μ M quinine. Quinine is an established high-affinity inhibitor of rOCT1 mediated transport (Koepsell et al., 2007). It inhibits rOCT1-mediated transport of

12.5 μM MPP⁺ into proteoliposomes to a similar degree as other high-affinity inhibitors of rOCT1 such as cyanine863 and tetrapentylammonium⁺ (Keller et al., 2005). 1-sec uptake of MPP⁺ was measured at 37°C in the absence and presence of quinine. 10 μl of prewarmed proteoliposomes (37°C) were mixed with 90 μl of prewarmed (37°C) NaC buffer (20 mM imidazole, pH 7.4, 0.1 μM Mg²⁺, 100 mM Na⁺, 100 mM cyclamate⁻) which contained different concentrations of MPP⁺ that were traced with [³H]MPP⁺. Proteoliposomes pretreated with quinine were incubated in the presence of 100 μM quinine. 1-sec incubation was performed as described as follows: The proteoliposomes were placed at the inner wall of the reaction tube just above the incubation medium. Uptake was initiated by mixing on a switched-on vortexer and stopped after 1 s by adding ice-cold stop solution (KC buffer containing 100 μM quinine) via a prepositioned pipette. A metronome was used to perform the 1-sec incubation measurements. Radioactivity was determined by washing the proteoliposomes on 0.22- μm cellulose acetate filters and liquid scintillation counting of the solubilized filters. MPP⁺ uptake was corrected for MPP⁺ uptake measured in the presence of quinine.

SDS-PAGE and Western blotting. Samples were incubated for 30 min at 37°C in 60 mM Tris-HCl, pH 6.8, containing 2% (w/v) SDS, 7% (v/v) glycerol, and 100 mM dithiothreitol. SDS-polyacrylamide gel electrophoresis (SDS-PAGE), staining of gels with Coomassie Brilliant Blue, and electroblotting to a polyvinylidene difluoride membrane were performed as described (Keller et al., 2008). For immunostaining of GFP-rOCT1 or mutants of GFP-rOCT1 an antibody against the large extracellular loop of rOCT1 raised in rabbit and goat anti-rabbit IgG coupled to horseradish peroxidase were used (Meyer-Wentrup et al., 1998). Binding of horseradish peroxidase-coupled IgG was visualized using enhanced chemiluminescence (ECL

system; Amersham Buchler, Braunschweig, Germany). Prestained molecular weight markers (BenchMark, Invitrogen) were used to determine apparent molecular masses.

Estimation of transporter in nanodiscs. In NDs coupled to Ni²⁺-NTA-agarose beads that were used for MPP⁺ binding measurements the concentrations of GFP-rOCT1 wildtype or GFP-rOCT1 mutants were determined by analysis of total protein (P_{total}) in combination with densitometry of Coomassie stained SDS polyacrylamide gels. Since the preparation consisted of empty NDs which only contained MSP1E3D1 protein or loaded NDs which only contained MSP1E3D1 and GFP-rOCT1 wildtype or one of the GFP-rOCT1 mutants (see Fig. 1B) the protein concentration of GFP-fusion (P_{GFP-F}) protein could be calculated as follows:

$$P_{\text{GFP-F}} = P_{\text{total}} \times S_{\text{GFP-F}} / (S_{\text{MSP1E3D1}} + S_{\text{GFP-F}})$$

Where P_{total} represents the total protein concentration, S_{GFP-F} staining of the respective GFP fusion protein, and S_{MSP1E3D1} staining of MSP1E3D1. Staining of proteins in Coomassie stained gels was quantified by densitometry using the program ImageJ (version 140g) supplied by the National Institute of Health. It was verified that the obtained staining intensities of GFP-rOCT1 and MSP1E3D1 were equally correlated with protein concentrations (Supplemental Fig. 2).

In silico docking of MPP⁺ to models of rOCT1. *In silico* docking was performed to outward-facing and inward-facing homology models of rOCT1 (Popp et al., 2005; Volk et al., 2009). All docking simulations were performed using the software package SYBYL version 7.1 (Tripos Inc, Saint Louis, MO) and employing the force field MMFF94s. A coordinate file of the organic cation MPP⁺ was built in SYBYL assuming standard geometry deduced from its 2D smiles description, hydrogen atoms were added to the initial coordinate set and the 3D structure of MPP⁺ was

subsequently energy-minimized employing a conjugate gradient algorithm. The models of rOCT1 in its inward and outward-facing conformation were complemented with hydrogens, partial charges were assigned using the AMBER7 FF02 force field (SYBYL version 7.1) and the rOCT1 structures carrying all-hydrogens were subsequently energy-minimized with the positions of all heavy atoms restrained by a strong positional harmonic potential employing a conjugate gradient algorithm. Docking simulations of MPP⁺ to both conformations of the rOCT1 model were performed using the FlexX module of the software SYBYL version 7.1. For the simulations, the side chains of lysine residues were protonated, the carboxylate groups of aspartic and glutamic acid residues were non-protonated, and cysteine and histidine residues were treated neutral. In a first round of docking simulations any site in the interior of the inward- or outward-facing cleft was accepted and the results were sorted according to their docking energies using the corresponding total FlexX-Scores. Since many docked MPP molecules were found in close proximity of residues Trp218, Arg440 and Asp475, a second round of docking simulations were performed with the docking restrained to be considered successful only when it occurred within a 7Å radius around these three residues. Again the results were sorted according to their docking energy and the top thirty results were analyzed.

Statistics. To determine the concentration dependence of MPP⁺ binding to GFP-rOCT1 wildtype or GFP-rOCT1 mutants reconstituted into NDs or transporter-mediated MPP⁺ uptake into proteoliposomes three independent experiments were performed in which 8-11 different MPP⁺ concentrations were analyzed and three parallel measurements were performed per experimental condition. A one-site or two-site binding model was fitted to the binding data and the Michaelis Menten equation to the uptake data of individual experiments. Mean values \pm S.D. of three

experiments are presented. The software package GraphPad Prism Version 4.1 (GraphPad Software, San Diego) was used to compute statistical parameters. When more than two groups were compared, the statistical significance of differences was determined by one-way ANOVA with post hoc Dunnett comparison (effects of mutants on binding or transport) or by two-way ANOVA with Bonferroni correction (comparison between effects of mutants on binding versus transport). When two individual groups were compared the Student's t-test was used. $P < 0.05$ was considered statistically significant. The curves presented in the figures were obtained by fitting the one-site or two-site model or the Michaelis Menten equation to the compiled data sets.

Results

Identification of Two MPP⁺ Binding Sites per rOCT1 Monomer in Nanodiscs Formed with 1,2-dimyristoyl-phosphoglycerol. For reconstitution of rOCT1 into NDs we performed cell-free expression of His-tagged rOCT1 fusion protein with a non-dimerizing mutant of green fluorescent protein (Zacharias et al., 2002) (GFP-rOCT1) in the absence of detergent and presence of empty NDs (Roos et al., 2013). The N-terminal fusion of rOCT1 with GFP did not impair the transport activity because the apparent K_m value for MPP⁺ uptake determined after reconstitution of GFP-rOCT1 into proteoliposomes was similar to the apparent K_m after reconstitution of purified rOCT1 (Keller et al., 2005; Keller et al., 2008). Empty NDs were formed by detergent removal from 1,2-dimyristoyl-*sn*-[phospho-*rac*-(1-glycerol)] (DMPG) and His-tagged membrane scaffold protein variant MSP1E3D1 that had been dissolved with dodecyl-phosphocholine (Denisov et al., 2004; Roos et al., 2012). When cell-free

expression in the absence of detergent was performed without addition of NDs, GFP-rOCT1 and some free GFP were observed in a 22,000×g pellet (Fig. 1A, see left P). After cell-free expression in the presence of empty NDs, NDs with reconstituted GFP-rOCT1 appeared in the 22,000×g supernatant whereas the amount of GFP-rOCT1 in the 22,000×g pellet was decreased (Fig. 1A, see S and P). For binding measurements, the NDs in the supernatant were purified with Ni²⁺-NTA agarose beads (Fig. 1B, see GFP-rOCT1, NDs). This preparation contained two proteins, the nanodisc component MSP1E3D1 (see MSP in Fig. 1) and GFP-rOCT1. Densitometric analysis revealed that GFP-rOCT1 represented $1.8 \pm 0.3\%$ ($n = 6$) of the total protein (Supplementary Table 1). Assuming that each GFP-rOCT1 containing nanodisc includes two MSP1E3D1 molecules and one GFP-rOCT1 monomer (Roos et al., 2013) about 1% of the NDs contained GFP-rOCT1. Considering the low percentage of NDs containing reconstituted transporter, the absence of posttranslational modifications after cell-free expression, and the reconstitution of GFP-rOCT1 into NDs in the absence of detergent, it is probable that the NDs containing GFP-rOCT1 represent a homogeneous population.

For binding measurements samples were incubated with radioactively labeled MPP⁺ for 1 min at 37°C and washed on cellulose acetate filters. Low nonspecific binding of MPP⁺ to filters, to agarose beads, to GFP linked to agarose beads, and to empty NDs linked to agarose beads was observed (Fig. 2A). In contrast, we observed distinct saturable MPP⁺ binding to agarose linked NDs containing GFP-rOCT1 (Fig. 2A, B). Binding of [³H]MPP⁺ to GFP-rOCT1 containing NDs in the presence of 2 mM nonradioactive MPP⁺ was not statistically significant higher compared to [³H]MPP⁺ binding to filters. 2.1 ± 0.1 MPP⁺ binding sites per rOCT1 monomer in the NDs were determined that have similar apparent K_D values which

could not be discriminated. For these sites a common value of $32 \pm 3.8 \mu\text{M}$ was determined (Fig. 2B, Table 1). For agarose coupled NDs containing GFP fusion protein with the non-oligomerizing rOCT1 variant GFP-rOCT1(6 Δ C) (Keller et al., 2011) a similar common apparent K_D value and the same number of MPP⁺ binding sites per transporter monomer were obtained (Fig. 2B, Table 1). This indicates that the determined number and affinity of MPP⁺ binding sites of rOCT1 reflect properties of transporter monomers. Measurements of MPP⁺ binding to GFP-rOCT1 at 0°C revealed 1.2 ± 0.1 MPP⁺ molecules per monomer and an apparent K_D value of $66 \pm 3.1 \mu\text{M}$ (Fig. 2B, Table 1). This suggests that a reduced conformational flexibility of the transporter at 0°C prevents access to one MPP⁺ binding site or impedes access to both identified MPP⁺ binding sites.

Trp218 and Asp475 are Involved in MPP⁺-binding to the Same Low-affinity MPP⁺ Binding Site. Previously we observed that exchange of Phe160 and Trp218 that were localized to outward- and inward-facing clefts of three-dimensional (3D) homology models of rOCT1, by tyrosine increased and decreased the apparent K_m value for MPP⁺, respectively (Popp et al., 2005; Gorboulev et al., 2018). When Asp475, the neighboring residue of Trp218 in the 3D model of the outward-facing cleft, was replaced by glutamate, the apparent K_m for MPP⁺ remained unchanged. In the present study we introduced the F160Y, W218Y or D475E mutation into GFP-rOCT1 and measured MPP⁺ binding to the mutants in NDs formed with DMPG (Fig. 2C-F, Table 1). The mutations had no effect on incorporation of the GFP-fusion proteins into the NDs (Supplementary Table 1). Similar to the apparent K_m value, the apparent K_D value for MPP⁺ binding to the GFP-rOCT1 mutants compared to wildtype was increased in mutant F160Y, whereas it was apparently decreased in mutant W218Y (see Table 1). Noteworthy, in mutants W218Y and D475E the maximal

binding (B_{\max}) of about two MPP⁺ molecule per monomer observed in wildtype rOCT1 was decreased to about one. To determine whether both mutations decrease MPP⁺ binding at the same site, we measured MPP⁺ binding to the double mutant W218Y/D475E. Like in both single mutants, a B_{\max} of about one per transporter monomer was observed suggesting that both mutations prevent MPP⁺ binding to the same site.

Identification of Three MPP⁺ Binding Sites per rOCT1 Monomer in Nanodiscs Formed with 1-palmitoyl-2-oleoyl-*sn*-glycero-3-phosphocholine or PC, PS and Cholesterol. Wondering why the previously described high-affinity binding site for MPP⁺ (Gorbunov et al., 2008) was not detected after reconstitution of GFP-rOCT1 in NDs formed with DMPG, we measured MPP⁺ binding to GFP-rOCT1 in NDs formed with 1,2-dipalmitoyl-*sn*-glycero-3-phosphocholine (DPPC) and 1-palmitoyl-2-oleoyl-*sn*-glycero-3-phosphocholine (POPC). With these lipids formation of NDs and incorporation of GFP-rOCT1 into NDs was similar as with DMPG (Supplemental Table 1, Supplemental Fig. 3). In NDs formed with DPPC a similar apparent K_D value ($25.6 \pm 3.1 \mu\text{M}$ versus $31.2 \pm 3.8 \mu\text{M}$, $n = 3$ each) and a slightly higher B_{\max} per monomer were observed compared to NDs formed with DMPG (2.35 ± 0.12 versus 2.08 ± 0.07 ($n = 3$ each, $P < 0.01$)). When GFP-rOCT1 was reconstituted into NDs formed with 1-palmitoyl-2-oleoyl-*sn*-glycero-3-phosphocholine (POPC), one high-affinity site ($B_{\max (\text{high aff.})} 0.93 \pm 0.05$) with an apparent K_D of $0.23 \pm 0.02 \mu\text{M}$ ($K_D (\text{high aff.})$) could be identified per transporter monomer in addition to two low-affinity sites ($B_{\max (\text{low aff.})} 2.29 \pm 0.05$) (Fig. 3A, Table 2). Similar to NDs formed with DMPG or DPPC, the affinities of the two low-affinity sites could not be discriminated and a common apparent K_D value ($36 \pm 2.6 \mu\text{M}$) was determined. The properties of GFP-rOCT1 in NDs formed with POPC are independent from dimerization because high-

and low-affinity MPP⁺ binding sites with similar properties were obtained after reconstitution of GFP-rOCT1 and GFP-rOCT1(6ΔC) (Table 2). The data indicate that an optimal lipid environment is required for accessibility of MPP⁺ to the high-affinity MPP⁺ binding site.

Next, we determined whether the nontransported inhibitor tetrabutylammonium⁺ (TBA⁺) (Gorboulev et al., 2018) blocks the identified MPP⁺ binding sites. TBA⁺ inhibits rOCT1 mediated MPP⁺ uptake into proteoliposomes with an *IC*₅₀ value of 19 μM (Keller et al., 2005). In NDs formed with POPC containing GFP-rOCT1, we measured the concentration dependence of MPP⁺ binding in the presence of 2 mM TBA⁺ (Supplemental Fig. 4). In the presence of 2 mM TBA⁺, 98% of MPP⁺ binding to the high-affinity site in the NDs and 75% of MPP⁺ binding to the low-affinity sites was blocked.

Previously we characterized MPP⁺ uptake into proteoliposomes which were generated from cell-free-expressed GFP-rOCT1 and equal weight mixtures of phosphatidylserine from egg yolk (PS), phosphatidylcholine from bovine brain (PC) and cholesterol (Keller et al., 2008). To evaluate whether the failure to distinguish a high-affinity *K_m* value for MPP⁺ uptake in proteoliposomes can be due to inaccessibility of the high-affinity MPP⁺ binding site in this lipid environment, we reconstituted GFP-rOCT1 also into NDs formed with the PS/PC/cholesterol mixture. Under these conditions one high-affinity MPP⁺ binding site per transporter monomer (*B*_{max} (high aff.) 1.01 ± 0.19) and two low-affinity MPP⁺ binding sites per monomer (*B*_{max} (low aff.) 2.06 ± 0.19) were determined as well (Fig. 4). The apparent *K_D* of the high-affinity binding site (0.16 ± 0.07 μM) was similar to NDs formed from POPC (0.23 ± 0.02 μM). At variance, for binding of MPP⁺ to the two low-affinity sites a lower common apparent *K_D* value compared to NDs formed from POPC was obtained (9.9

$\pm 2.8 \mu\text{M}$ versus $36 \pm 2.6 \mu\text{M}$, $P < 0.001$, $n = 3$ each). Noteworthy, the apparent low-affinity K_D value for MPP⁺ binding measured in NDs formed with PS/PC/cholesterol mixture is lower compared to the apparent K_m value measured in proteoliposomes formed with the same lipids (see Table 2, $9.9 \pm 2.8 \mu\text{M}$ versus $19.3 \pm 3.1 \mu\text{M}$, $P < 0.001$, $n = 3$ each).

Evidence that Arg440 is Involved in MPP⁺-binding to a Different Low-affinity MPP⁺ Binding Site than Trp218 and Asp475. To determine whether the mutations studied in NDs formed with DMPG exhibit effects on the high-affinity MPP⁺ binding site, we also measured MPP⁺ binding after reconstitution of the mutants in NDs formed with POPC (Fig. 3B, D, E, Fig. 5A, Table 2). In NDs formed with POPC the mutations F160Y, W218Y, D475E and the double mutant W218Y/D475E exerted similar effects on low-affinity MPP binding as in NDs formed with DMPG. B_{max} of low-affinity MPP⁺ binding per monomer was reduced from about two to one in mutants W218Y, D475E and W218Y/D475E and the affinity for low-affinity binding was decreased in mutant F160Y. B_{max} for high-affinity binding remained unaltered. The apparent K_D for high-affinity binding of MPP⁺ was increased in mutant W218Y suggesting an allosteric effect of this mutation on the high affinity MPP⁺ binding site.

Trying to localize the second low-affinity and the high-affinity MPP⁺ binding site, we also analysed mutations of Arg440, Leu447 and Gln448 which have been also localized within the outward-open cleft of our rOCT1 model (Gorboulev et al., 2018; Volk et al., 2009) (Fig. 3C, Fig. 5B,C,D, Table 2). In mutants L447Y, L447F and Q448E maximal binding to the low- and high-affinity binding sites per monomer was not altered, however, the apparent K_D values for low-affinity binding were decreased. The data indicate that Leu447 and Gln448 are not essential for low- or high-affinity binding, but that mutations in these positions may exhibit allosteric effects on MPP⁺

binding sites. After replacement of Arg440 by lysine B_{\max} of low-affinity binding was decreased from 2.29 ± 0.05 to 1.24 ± 0.06 per monomer (Fig. 3C, Table 2). The common apparent K_D value for low-affinity binding of MPP⁺ was doubled, whereas high-affinity binding remained unchanged. To determine whether the R440K mutation blunted MPP⁺ binding to a different low-affinity site than the D475E mutation, we measured MPP⁺ binding to double mutant R440K/D475E (Fig. 3F, Table 2). Noteworthy in this mutant no low-affinity MPP⁺ binding was detectable whereas B_{\max} per transporter monomer of high-affinity MPP⁺ binding was not altered.

Evidence that Both Low-affinity MPP⁺ Binding Sites are Involved in Transport. To elucidate the relevance of the MPP⁺ binding sites for transport, we reconstituted cell-free-expressed GFP-rOCT1 wildtype and GFP-rOCT1 mutants into proteoliposomes and measured the substrate dependence of MPP⁺ uptake. The proteoliposomes were formed from PS, PC and cholesterol and MPP⁺ uptake was measured after 1-sec incubation at 37°C in the presence of an inside-negative potassium diffusion potential as described for rOCT1 (Keller et al., 2008). Similar to rOCT1 in proteoliposomes (Keller et al., 2005; Keller et al., 2008) and to rOCT1 expressed in oocytes or human embryonic kidney (HEK) 293 cells (Busch et al., 1996; Gorboulev et al., 2018) for GFP-rOCT1 in proteoliposomes a hyperbolic concentration dependence was observed that could be fitted to Michaelis Menten equation (Fig. 6A). No indication for an additional high-affinity uptake was detectable. For GFP-rOCT1 an apparent K_m value of 19 ± 3.1 μ M ($n = 3$) was obtained which was lower than the apparent K_m of 35 ± 1.5 μ M determined for cell-free-expressed rOCT1 in proteoliposomes (Keller et al., 2008).

In mutants W218Y and R440K, where binding of MPP⁺ to one or the other low-affinity binding site was largely impaired, and which led to 41% (W218Y) and 46%

(R440K) decrease of total low-affinity binding, the V_{\max} of MPP⁺ transport was reduced by 44% (W218Y) and 29% (R440K) (Fig. 6B, C, Fig. 7A, Table 2). When the Trp218- and Asp475-related binding site was blocked by exchange of Asp475 with glutamate, total low-affinity binding was decreased by 44% similar to the W218Y mutation, however, a more pronounced 79% decrease of V_{\max} was observed (Fig. Fig. 6E, Fig. 7A, Table 2). The more pronounced effect on V_{\max} reflects the dual role of Asp475 for substrate affinity and transport related conformational changes (Egenberger et al., 2012). The double mutant W218Y/D475E exhibited similar properties as the D475E mutant showing a 54% reduction of low-affinity binding and a 78% reduction of V_{\max} (Fig. 6D, Fig. 7A Table 2). In double mutant R440K/D475E, where no low-affinity binding was detected, the V_{\max} was reduced by 96% (Fig. 6F, Fig. 7A, Table 2). The data indicate that MPP⁺ binding to the two identified low-affinity sites is critically involved in translocation.

In mutants W218Y, D475E and W218Y/D475E the apparent K_m value for MPP⁺ uptake was not altered significantly, whereas in mutant R440K the apparent K_m value was increased 3fold (Fig, 7B). The effects on apparent K_m have some similarity to the effects on the common apparent K_D (low aff.) value which was not altered in mutant D475E, decreased by 42% in mutants W218Y and W218Y/D475E, and 2.3fold increased in mutant R440K. The small differences between the effects of the R440K and W218Y/D475E mutations on apparent K_m versus apparent K_D (low aff.) values (Fig. 7B) may reveal the difference in lipid composition between the NDs and proteoliposomes and/or that the affinity for substrate binding may not exclusively determine the K_m for translocation.

In mutants F160Y, L447Y, L447F and Q448E no significant changes of the determined total number of three binding sites per transporter monomer and the V_{\max}

values for MPP⁺ transport was observed (Fig. 5, Fig. 8, Table 2). However, apparent K_D (low aff.) and apparent K_m values were increased in mutant F160Y and decreased in mutants L447Y and L447F. The data support the interpretation that the investigated mutations of Phe160 and Leu447 induce allosteric effects on MPP⁺ binding to the low-affinity sites which are critically involved in translocation.

Docking of MPP⁺ to Modeled Outward- and Inward-open Clefts of rOCT1.

Previously we generated a 3D homology model of the inward-open conformation of rOCT1 on basis of the crystal structure of lactose permease from *Escherichia coli* that belongs to the MFS superfamily like the OCTs (Popp et al., 2005). In addition, we also built a 3D model of rOCT1 in the outward-open conformation by assuming a rigid-body movement of the six N-terminal helices of rOCT1 with respect to the six C-terminal helices similar as has been modeled and experimentally verified for lactose permease (Volk et al., 2009; Kaback et al., 2007; Holyoake and Sansom, 2007). Using crystal structures of various transporters of the MFS superfamily as templates, recently an outward-open 3D model of human OCT1 (hOCT1) was built (Dakal et al., 2017). In this hOCT1 model the locations of Phe160, Trp218, Arg440 and Asp475 within the outward-open cleft of rOCT1 were confirmed (Gorboulev et al., 2018). In the outward-open models of rOCT1 and hOCT1 Trp218 (Trp217 in hOCT1) and Asp475 (Asp474) in close proximity, whereas Arg440 (Arg439) is located more distantly to the two other residues. This is consistent with our mutagenesis data suggesting that Asp475 and Trp218 contribute to the same low-affinity MPP⁺ binding site, whereas Arg440 is important for integrity of the second low-affinity MPP⁺ binding site. In inward-open cleft model of rOCT1 Asp475 is located distantly from Trp218 and Arg440 (Volk et al., 2009). This suggests that in the reconstituted NDs MPP⁺ binding to the outward-open conformation has been analysed. Trying to obtain

additional insight on MPP⁺ binding close to Trp218, Arg440 and Asp475 we performed *in silico* docking simulations of MPP⁺ into the outward-facing and inward-facing clefts of our 3D homology models of rOCT1. To screen potential binding sites close to the above listed residues, docking was restrained to be within a 7Å radius around these residues. The docking simulations have been deposited at the Protein Model Database¹. The thirty docked MPP⁺ molecules with the highest docking energies in both conformations were analysed (Fig. 9). In the outward- and inward-open rOCT1 conformation 26 and 22 molecules were found docked within the cleft, respectively. In the outward-open cleft 18 MPP⁺ molecules were located close to Trp218 and Asp475, whereas in the inward-open conformation 10 MPP⁺ were close to both Trp218 and Asp475. Hence the docking experiments did not allow to decide whether low-affinity binding of two MPP⁺ molecules to the outward- or inward-open cleft has been determined by the binding measurements of GFP-rOCT1 in NDs.

Discussion

Based on mutagenesis experiments in rOCT1 combined with binding and transport measurements of the model cation MPP⁺ our study reveals novel insight into recognition and transport of drugs by polyspecific organic cation transporters (OCTs) of the *SLC22* transporter family. The experiments were performed with cell-free-expressed GFP-rOCT1 fusion protein that was reconstituted into NDs and proteoliposomes. Evidence is provided that each rOCT1 monomer contains two low-affinity MPP⁺ binding sites that are involved in MPP⁺ transport and one high-affinity MPP⁺ binding site that does not directly participate in transport but may mediate allosteric effects on the low-affinity MPP⁺ binding sites. It cannot be excluded that the

determined numbers of MPP⁺ binding sites per transporter monomer are underestimated because it has not been approved experimentally that all transporter monomers in the NDs have been functional. However, functionality of all transporters in our preparation is probable because the reconstitution of GFP-rOCT1 into NDs was performed by cotranslational insertion during cell-free expression of the transporter in the absence of detergent (Roos et al., 2013). Thus, posttranslational protein modifications and protein aggregation causing protein heterogeneities were avoided. More importantly, because only about 1% of the NDs contained GFP-rOCT1, a homogeneous population of NDs containing functional transporter is expected.

The identified high-affinity MPP⁺ binding site was only accessible in specific lipid environments, namely in NDs formed with POPC or a mixture of cholesterol, PC and PS, but not with DMPG or DPPC. The lipid dependence suggests that a minimal membrane fluidity (POPC versus DPPC) and/or an optimal membrane thickness (DMPG versus POPC) is required for an *in vivo*-like transporter conformation with an accessible high-affinity binding site. Phospholipid binding to a lipid binding site of rOCT1 as has been described for some transporters (Laganowsky et al., 2014), is also possible.

The individual involvement of the low-affinity sites in transport is concluded from an observed parallel decrease of B_{\max} of MPP⁺ binding and V_{\max} of MPP⁺ transport after inactivation of one or the other low-affinity MPP⁺ binding site in mutants W218Y and R440K and the total absence of uptake after inactivation of both low-affinity binding sites in the double mutant R440K/D475E. A direct involvement of the high-affinity MPP⁺ binding site in transport could be excluded because B_{\max} of high-affinity MPP⁺ binding remained unchanged when both low-affinity MPP⁺ binding sites were

blocked and MPP⁺ transport was abolished. In addition, neither a high-affinity MPP⁺ transport site nor positive cooperativity could be detected measuring the substrate dependence of MPP⁺ uptake in proteoliposomes (Fig. 6A) or in rOCT1 expressing oocytes, in which high-affinity MPP⁺ binding sites have been identified (Busch et al., 1996; Gorbunov et al., 2008).

The discovered properties of rOCT1 provide a molecular framework to understand how various factors can influence affinities of inhibitors. For example, for inhibition of MPP⁺ uptake into rOCT1-expressing HEK293 cells by a non-transported inhibitor largely different IC₅₀ values were obtained when different concentrations of MPP⁺ far below the apparent K_m for MPP⁺ uptake were used for uptake measurements (Gorbunov et al., 2018). Under these conditions only one low affinity MPP⁺ binding site is supposed to be involved in transport and a different occupation of the high affinity MPP⁺ binding site is assumed. Considering that OCTs contain not only partially overlapping binding sites for cationic drugs with largely different structures that are involved in transport or interact with transport-related sites (Koepsell, 2013), but also high-affinity cation binding sites (Minuesa et al., 2009; Gorbunov et al., 2008), a high complexity of drug-drug interaction is anticipated. Hence, the procedures recommended by the FDA and EMA and in the literature to determine whether NMEs interact with hOCT1 or hOCT2 by measuring inhibition of uptake of one concentration of MPP⁺ or metformin as test substrate are insufficient for drug development because effects of substrate structure and functional relevant high-affinity inhibition are missed (Koepsell, 2018). Considering the complexity of drug interactions with OCTs more sophisticated approaches are required. Hence, we suggest employing three structurally diverse substrates including a clinically relevant compound at three different concentrations far below the respective K_m values for *in*

vitro testing of NMEs by inhibition experiments. Pharmacophore models based on the different experimental conditions may be generated and applied one after the other to achieve a predictive potential that is high enough to justify *in silico* exclusion of NMEs from *in vitro* testing. Such line of action is mandatory for *in silico* prediction because so far described pharmacophore models for hOCT1 and hOCT2 which are based on uptake measurements performed at one substrate concentration close to the respective K_m value, are insufficient. By these models only between 70% and 82% of the interacting drugs have been identified (Koepsell, 2018).

The current molecular understanding how human polyspecific drug transporters recognize compounds with different molecular structures is limited because it is mainly based on modeling and on indirect experimental evidence. So far crystal structures of mammalian polyspecific transporters and of transporter-ligand complexes are missing and homology models derived from crystal structures of bacterial transporters belonging to the same superfamily and docking experiments of ligands to the homology models have only limited informative value. Extensive mutagenesis studies have only been performed with few polyspecific drug transporters measuring effects of mutations on apparent K_m values of substrates and on IC_{50} values for inhibition of transport. These measurements depict secondary effects of the mutations rather than direct effects on substrate- or inhibitor-binding. Recently crystal structures of four dipeptide complexes with different conformations of the proton-dependent peptide transporter PepT_{ST} from *Streptococcus thermophiles* have been reported (Martinez et al., 2018). The data suggest that binding of different dipeptides to PepT_{ST} occurs at the same binding site and is enabled by movements of the interacting amino acid residues in combination with adjustments of dipeptide positions and interposition of water molecules. Remarkably

the half maximal effective concentrations (EC_{50}) obtained for the interaction of the co-crystallized dipetides exhibiting different but not completely divergent structures with solubilized PepT_{StT} ranged between 0.56 mM and >50 mM. In contrast organic cations with completely different molecular structures such as TBuA⁺, metformin⁺ and MPP⁺ interact with OCTs, and EC_{50} values ranging between subnanomolar and millimolar concentrations have been determined. Consistent with this different degree of polyspecificity between proton-peptide cotransporters and OCTs, we provided evidence for the existence of different cation binding sites in rOCT1. Each of these binding sites in rOCT1 - and presumably different binding sites in all OCTs - may recognize a group of structurally related compounds employing mechanisms as described for PepT_{StT}. In total this allows the recognition of a large variety of structurally diverse compounds by OCTs.

Measuring binding of MPP⁺ to GFP-rOCT1 in NDs, binding to low-affinity binding sites either within the outward-open or the inward-open cleft of the transporter is determined. On basis of homology modeling and docking data no distinction between binding to the outward-open and inward-open cleft can be made. Likewise, the determined apparent K_m values for MPP⁺ uptake and the apparent K_D values for low-affinity MPP⁺ binding do not allow a distinction between binding to the outward- or inward-open cleft because we do not know whether rOCT1-mediated cellular influx and efflux of MPP⁺ are asymmetric and have different K_m values for MPP⁺ transport and/or different K_D values for low-affinity MPP⁺ binding. The observation that apparent K_m values of 35 μ M and 19 μ M for MPP⁺ uptake in proteoliposomes containing cell-free expressed rOCT1 (Keller et al. 2008) or GFP-rOCT1 were higher than the apparent K_m values measured for rOCT1 mediated MPP⁺ uptake in oocytes (4.9 μ M) and HEK293 cells (3.9 μ M) could indicate that rOCT1 in the

proteoliposomes is oriented inside-out and the K_m for MPP⁺ efflux is higher compared to influx, however, different properties of rOCT1 in proteoliposomes compared to rOCT1 in native plasma membranes cannot be excluded. Because a high-affinity MPP⁺ binding site on rOCT1 expressed in oocytes has been identified after short-term extracellular application of MPP⁺ (Gorbunov et al., 2008), it is highly probable that the detected high-affinity MPP⁺ binding site is accessible from extracellular. The MPP⁺ docking experiment to the outward-open cleft is consistent with the interpretation that the high-affinity and the two low-affinity MPP⁺ binding sites are located within the outward-open cleft.

In summary, the data described in this paper provide a rationale to improve *in vitro* and *in silico* testing of NMEs for interaction with OCTs. Demonstrating three different binding sites for one substrate in one rOCT1 monomer in combination with the property of OCTs to translocate structurally diverse compounds, it is concluded that these highly polyspecific transporters contain various binding sites that are mostly or exclusively located within the large clefts that may be exposed to extracellular or intracellular. Future attempts to crystallize transporters of the *SLC22* family that are performed in the presence of structurally different ligands and lipids containing unsaturated fatty acids and/or cholesterol may be successful. The demonstration of one high-affinity and two low-affinity binding sites in rOCT1 and the identification of amino acids which participate in formation of the low-affinity binding sites will help to interpret obtained crystal structures.

Acknowledgements

We thank Martin Lohse (Institute of Pharmacology and Toxicology, University Würzburg) for providing laboratory space and giving technical support and Michael Christof (Institute of Anatomy and Cell Biology, University Würzburg) for preparing the figures.

Author Contributions

Research design: Keller, Mueller, Bernhard, Koepsell

Conducted experiments: Keller, Gorboulev, Mueller, Bernhard

Supplied experimental tools: Bernhard, Dötsch

Performed data analysis: Keller, Mueller, Koepsell

Wrote the manuscript: Koepsell

REFERENCES

- Ahlin G, Chen L, Lazorova L, Chen Y, Ianculescu AG, Davis RL, Giacomini KM, and Artursson P (2011). Genotype-dependent effects of inhibitors of the organic cation transporter, OCT1: predictions of metformin interactions. *Pharmacogenomics J* **11**:400-411.
- Ahlin G, Karlsson J, Pedersen JM, Gustavsson L, Larsson R, Matsson P, Norinder U, Bergström CAS, and Artursson P (2008). Structural requirements for drug inhibition of the liver specific human organic cation transport protein. *J Med Chem*:5932-5942.
- Amphoux A, Vialou V, Drescher E, Brüss M, La Cour CM, Rochat C, Millan MJ, Giros B, Bönisch H, and Gautron S (2006). Differential pharmacological in vitro properties of organic cation transporters and regional distribution in rat brain. *Neuropharmacology* **50**:941-952.
- Belzer M, Morales M, Jagadish B, Mash EA, and Wright SH (2013). Substrate-dependent ligand inhibition of the human organic cation transporter OCT2. *J Pharmacol Exp Ther* **346**:300-310.
- Brast S, Grabner A, Sucic S, Sitte HH, Hermann E, Pavenstadt H, Schlatter E, and Ciarimboli G (2012). The cysteines of the extracellular loop are crucial for trafficking of human organic cation transporter 2 to the plasma membrane and are involved in oligomerization. *FASEB J* **26**:976-986.
- Budiman T, Bamberg E, Koepsell H, and Nagel G (2000). Mechanism of electrogenic cation transport by the cloned organic cation transporter 2 from rat. *J Biol Chem* **275**:29413-29420.

- Busch AE, Quester S, Ulzheimer JC, Waldegger S, Gorboulev V, Arndt P, Lang F, and Koepsell H (1996). Electrogenic properties and substrate specificity of the polyspecific rat cation transporter rOCT1. *J Biol Chem* **271**:32599-32604.
- Chen EC, Khuri N, Liang X, Stecula A, Chien HC, Yee SW, Huang Y, Sali A, and Giacomini KM. (2017). Discovery of competitive and noncompetitive ligands of the organic cation transporter 1 (OCT1; SLC22A1). *J Med Chem* **60**:2685-2696.
- Dakal TC, Kumar R, and Ramotar D (2017). Structural modeling of human organic cation transporters. *Comput Biol Chem* **68**:153-163.
- Denisov IG, Grinkova YV, Lazarides AA, and Sligar SG (2004). Directed self-assembly of monodisperse phospholipid bilayer nanodiscs with controlled size. *J Am Chem Soc* **126**:3477-3487.
- Egenberger B, Gorboulev V, Keller T, Gorbunov D, Gottlieb N, Geiger D, Mueller TD, and Koepsell H (2012). A substrate binding hinge domain is critical for transport-related structural changes of organic cation transporter 1. *J Biol Chem* **287**:31561-31573.
- EMA (2012). Guideline on investigation of drug interactions. http://www.ema.europa.eu/en/docs/en_GB/document_library/Scientific_guideline/2012/07/WC500129606.pdf.
- FDA (2017) Draft guidance for in vitro metabolism and transporter mediated drug-drug interaction studies. Guidance for industry. <https://www.fda.gov/downloads/Drugs/GuidanceComplianceRegulatoryInformation/Guidance/UCM581965.pdf>.
- Giacomini KM, Huang S-M, Tweedie DJ, Benet LZ, Brouwer KL, Chu X, Dahlin A, Evers R, Fischer V, Hillgren KM, Hoffmaster KA, Ishikawa T, Keppler D, Kim RB, Lee CA, Niemi M, Polli JW, Sugiyama Y, Swaan PW, Ware JA, Wright SH, Yee

- SW, Zamek-Gliszczynski MJ, and Zhang L (2010). Membrane transporters in drug development. *Nat Rev Drug Discov* **9** :215-236.
- Gorboulev V, Rehman S, Albert CM, Roth U, Meyer MJ, Tzvetkov MV, Mueller TD, and Koepsell H (2018). Assay conditions influence affinities of rat organic cation transporter 1: Analysis of mutagenesis in the modeled outward-facing cleft by measuring effects of substrates and inhibitors on initial uptake. *Mol Pharmacol* **93**:402-415.
- Gorboulev V, Shatskaya N, Volk C, and Koepsell H (2005). Subtype-specific affinity for corticosterone of rat organic cation transporters rOCT1 and rOCT2 depends on three amino acids within the substrate binding region. *Mol Pharmacol* **67**:1612-1619.
- Gorboulev V, Volk C, Arndt P, Akhoundova A, and Koepsell H (1999). Selectivity of the polyspecific cation transporter rOCT1 is changed by mutation of aspartate 475 to glutamate. *Mol Pharmacol* **56**:1254-1261.
- Gorbunov D, Gorboulev V, Shatskaya N, Mueller T, Bamberg E, Friedrich T, and Koepsell H (2008). High-affinity cation binding to organic cation transporter 1 induces movement of helix 11 and blocks transport after mutations in a modeled interaction domain between two helices. *Mol Pharmacol* **73**:50-61.
- Holyoake J, and Sansom MSP (2007). Conformational change in an MFS protein: MD simulations of LacY. *Structure* **15**:873-884.
- Kaback HR, Dunten R, Frillingos S, Venkatesan P, Kwaw I, Zhang W, and Ermolova, N (2007). Site-directed alkylation and the alternating access model for LacY. *Proc Natl Acad Sci USA* **104**:491-494.
- Keller T, Egenberger B, Gorboulev V, Bernhard F, Uzelac Z, Gorbunov D, Wirth C, Koppatz S, Dötsch V, Hunte C, Sitte HH, and Koepsell H (2011). The large

extracellular loop of organic cation transporter 1 influences substrate affinity and is pivotal for oligomerization. *J Biol Chem* **286**:37874-37886.

Keller T, Elfeber M, Gorboulev V, Reiländer H, and Koepsell H (2005). Purification and functional reconstitution of the rat organic cation transporter OCT1. *Biochemistry* **44**:12253-12263.

Keller T, Schwarz D, Bernhard F, Dötsch V, Hunte C, Gorboulev V, and Koepsell H (2008). Cell-free expression and functional reconstitution of eukaryotic drug transporters. *Biochemistry* **47**:4552-4564.

Klammt C, Löhr F, Schäfer B, Haase W, Dötsch V, Rüterjans H, Glaubitz C, and Bernhard F. (2004). High level cell-free expression and specific labeling of integral membrane proteins. *Eur J Biochem* **271**:568-580.

Koepsell H (2013). The SLC22 family with transporters of organic cations, anions and zwitterions. *Mol Aspects Med* **34**:413-435.

Koepsell H, Lips K, and Volk C (2007). Polyspecific organic cation transporters: structure, function, physiological roles, and biopharmaceutical implications. *Pharm Res* **24**:1227-1251.

Koepsell H (2018). Multiple binding sites in organic cation transporters require sophisticated procedures to identify interactions of novel drugs. *Biol Chem* doi: 10.1515/hsz-2018-0191.

Laganowsky A, Reading E, Allison TM, Ulmschneider MB, Degiacomi MT, Baldwin AJ, and Robinson CV (2014) Membrane proteins bind lipids selectively to modulate their structure and function. *Nature* **510**:172–175.

Martinez MM, Quistgaard EM, Flayhan A, Pieprzyk J, and Low C (2018). Multispecific substrate recognition in a proton-dependent oligopeptide transporter. *Structure* **26**:467–476.

- Meyer-Wentrup F, Karbach U, Gorboulev V, Arndt P, and Koepsell H (1998). Membrane localization of the electrogenic cation transporter rOCT1 in rat liver. *Biochem Biophys Res Commun* **248**:673-678.
- Minuesa G, Albert C, Pastor-Anglada M, Martinez-Picado J, and Koepsell H. (2017). Response to "Tenofovir disoproxil fumarate is not an inhibitor of human organic cation transporter 1". *J Pharmacol Exp Ther* **360**:343-345.
- Minuesa G, Huber-Ruano I, Pastor-Anglada M, Koepsell H, Clotet B, and Martinez-Picado J (2011). Drug uptake transporters in antiretroviral therapy. *Pharmacol. Ther* **132**:268-279.
- Minuesa G, Volk C, Molina-Arcas M, Gorboulev V, Erkizia I, Arndt P, Clotet B, Pastor-Anglada M, Koepsell H, and Martinez-Picado J (2009). Transport of lamivudine [(-)-b-L-2',3'-dideoxy-3'-thiacytidine] and high-affinity interaction of nucleoside reverse transcriptase inhibitors with human organic cation transporters 1, 2, and 3. *J Pharmacol Exp Ther* **329**:252-261.
- Nies AT, Koepsell H, Damme K, and Schwab M (2010). Organic cation transporters (OCTs, MATEs), in vitro and in vivo evidence for the importance in drug therapy. *Handb Exp Pharmacol* **201**:105-167.
- Popp C, Gorboulev V, Müller TD, Gorbunov D, Shatskaya N, and Koepsell H (2005). Amino acids critical for substrate affinity of rat organic cation transporter 1 line the substrate binding region in a model derived from the tertiary structure of lactose permease. *Mol Pharmacol* **67**:1600-1611.
- Roos C, Kai L, Proverbio D, Ghoshdastider U, Filipek S, Doetsch V, and Bernhard F (2013). Co-translational association of cell-free expressed membrane proteins with supplied lipid bilayers. *Mol Membr Biol* **30**:75-89.

- Roos C, Zocher M, Muller D., Munch D, Schneider T, Sahl HG, Scholz F, Wachtveitl J, Ma Y, Proverbio D, Henrich E, Dötsch, V, and Bernhard F (2012). Characterization of co-translationally formed nanodisc complexes with small multidrug transporters, proteorhodopsin and with the E. coli MraY translocase. *Biochim Biophys Acta* **1818**:3098-3106.
- Sandoval PJ, Zorn KM, Clark AM, Ekins S, and Wright SH (2018). Assessment of substrate dependent ligand interactions at the organic cation transporter OCT2 using six model substrates. *Mol Pharmacol* **94**: 1057-1068.
- Schmitt BM and Koepsell H (2005). Alkali cation binding and permeation in the rat organic cation transporter rOCT2. *J Biol Chem* **280**:24481-24490.
- Suhre WM, Ekins S, Chang C, Swaan PW, and Wright SH. (2005). Molecular determinants of substrate/inhibitor binding to the human and rabbit renal organic cation transporters hOCT2 and rbOCT2. *Mol Pharmacol* **67**:1067-1077.
- Thevenod F, Ciarimboli G, Leistner M, Wolff NA, Lee WK, Schatz I, Keller T, Al-Monajjed R, Gorboulev V, and Koepsell H. (2013). Substrate- and cell contact-dependent inhibitor affinity of human organic cation transporter 2: studies with two classical organic cation substrates and the novel substrate Cd²⁺. *Mol Pharm* **10**:3045-3056.
- U.S. Food and Drug Administration (2012) Guidance for industry: Drug interaction studies - study design, data analysis, implications for dosing, and labeling recommendations, (Huang, S.M. and Zhang, L. eds) pp 1-79.
- U.S. Food and Drug Administration (2017) Guidance for industry: In vitro metabolism- and transporter-mediated drug-drug interaction studies. pp 1-47.
- Volk C, Gorboulev V, Kotzsch A, Müller TD, and Koepsell H (2009). Five amino acids in the innermost cavity of the substrate binding cleft of organic cation transporter 1

interact with extracellular and intracellular corticosterone. *Mol Pharmacol* **76**:275-289.

Yin Y, Duan D, and Wang J (2016). Impact of substrate-dependent inhibition on renal cation transporters hOCT2 and MATE1/2-K-mediated drug transport and intracellular accumulation. *J Pharmacol Exp Ther* **359**:401-410.

Zacharias DA, Violin JD, Newton AC, and Tsien RY (2002). Partitioning of lipid-modified monomeric GFPs into membrane microdomains of live cells. *Science* **296**:913-916.

Zamek-Gliszczynski MJ, Giacomini KM, and Zhang L (2018). Emerging clinical importance of hepatic organic cation transporter 1 (OCT1) in drug pharmacokinetics, dynamics, pharmacogenetic variability and drug interactions. *Clin Pharmacol Ther* 105, doi:10.1002/cpt.941.

Footnotes

This work was supported by the Deutsche Forschungsgemeinschaft (KO 862/6-1).

¹ Protein Model database (<https://bioinformatics.cineca.it/PMDB/main.php>):

Accession # PM0081570, MPP⁺ docking to the outward-open conformation of rOCT1; accession # PM0081569, MPP⁺ docking to inward-open conformation of rOCT1.

Legends to Figures

Fig. 1. Reconstitution of GFP-rOCT1 into nanodiscs formed with MSP1E3D1 and DMPG and their isolation. (A) Cell-free expression of His-tagged GFP-rOCT1 in absence or presence of empty NDs composed of DMPG and His-tagged MSP1E3D1 (MSP). An SDS-polyacrylamide gel stained with Coomassie brilliant blue is shown. Lanes R show proteins in reaction mixtures without and with NDs at the beginning of cell-free synthesis. After completion of the synthesis, the reaction mixtures were centrifuged for 20 min at 22,000×g. The supernatants are shown in lanes S and the pellets in lanes P. When the synthesis was performed in the presence of NDs some GFP-rOCT1 appeared in the supernatant, whereas the amount of GFP-rOCT1 in the pellet was decreased. (B) Preparation of NDs containing His-tagged GFP-rOCT1 which was employed for MPP⁺ binding measurements. Using Ni²⁺-NTA linked to agarose beads the His-tagged NDs were precipitated from the 22,000×g supernatant obtained after cell-free expression of GFP-rOCT1 in the presence of NDs. Purified GFP (pur. GFP), purified GFP-rOCT1 (pur. GFP-rOCT1), purified MSP1E3D1 (pur. MSP), empty NDs (empty NDs) and precipitated NDs with reconstituted GFP-rOCT1 (GFP-rOCT1, NDs) were separated by SDS-PAGE and stained with Coomassie brilliant blue (left panel) or visualized in a Western blot (right panel) which was developed with an antibody against rOCT1. 2 µg of protein were applied per lane.

Fig. 2. Binding of MPP⁺ to nanodiscs composed of DMPG and MSP1E3D1 containing wildtype GFP-rOCT1 and GFP-rOCT1 variants. (A) Characterization of MPP⁺ binding to nanodiscs (NDs). Binding of 12.5 nM [³H]MPP⁺ in the absence and presence of 2 mM nonradioactive MPP⁺ was measured at 37°C. Binding was measured to filters, Ni²⁺-NTA-agarose (agarose), GFP linked to Ni²⁺-NTA-agarose

(agarose, GFP), empty NDs linked to Ni²⁺-NTA-agarose (agarose, NDs), and a mixture of empty NDs and GFP-rOCT1 containing NDs linked to Ni²⁺-NTA-agarose (agarose, NDs, GFP-rOCT1). Identical amounts of agarose beads were analysed. Mean values \pm S.D. of four measurements are shown. ***P<0.001 Student's t-test.

(B) Effects of temperature and capability of rOCT1 to dimerize on MPP⁺ binding. MPP⁺ binding to GFP-rOCT1 (WT) containing NDs was measured at 37°C or 0°C, and MPP⁺ binding to non-dimerizing GFP-rOCT1(6ΔC) variant was measured at 37°C. Binding to filters was subtracted. Concentrations of rOCT1 and rOCT1(6ΔC) were determined by measuring total protein in combination with densitometry of stained gels. Mean values \pm S.D. of three experiments are indicated. The curves in the left panel were obtained by fitting a "one site binding" model to the data. The straight lines in the right panel were obtained by linear regression. (C-F) Concentration dependence of MPP⁺ binding to NDs containing mutants GFP-rOCT1(F160Y) (C), GFP-rOCT1(W218Y) (D), GFP-rOCT1(D475E) (E) or GFP-rOCT1(W218Y, D475E) (F). The measurements in C-F were performed and the data were calculated as in Fig. 2B.

Fig. 3. Binding of MPP⁺ to nanodiscs composed of POPC and MSP1E3D1 containing GFP-rOCT1 wildtype and mutants with amino acid exchanges in positions 218, 440 and 475. His-tagged GFP-rOCT1 (WT) or GFP-rOCT1 mutants were reconstituted by cell-free expression in the presence of empty NDs formed from POPC and His-tagged MSP1E3D1. The NDs were precipitated by Ni²⁺-NTA agarose and binding of 12.5 nM [³H]MPP⁺ was measured at 37°C in the presence of various concentration of unlabeled MPP⁺. MPP⁺ binding was measured and numbers of transporter monomers were determined as in Figure 2B. Mean values \pm S.D. of three

experiments are indicated. A two-site binding model was fitted to the data. In the right panels, MPP⁺ binding and the fitted curves at low MPP⁺ concentrations are shown.

Fig. 4. Binding of MPP⁺ to GFP-rOCT1 in Nanodiscs Formed with PC, PS and Cholesterol and MSP1E3D1. His-tagged GFP-rOCT1 was reconstituted by cell free expression in the presence of empty NDs formed from PC, PS and cholesterol and His-tagged MSP1E3D1. The NDs were precipitated by Ni²⁺-NTA agarose beads and binding of 12.5 nM [³H]MPP⁺ was measured at 37°C in the presence of various concentrations of unlabeled MPP⁺. MPP⁺ binding was measured and numbers of transporter monomers were determined as in Figure 2B. Mean values ± S.D. of three experiments are indicated. A two-site binding model was fitted to the data. In the right panels, MPP⁺ binding and the fitted curves at low MPP⁺ concentrations are shown.

Fig. 5. Binding of MPP⁺ to nanodiscs composed of POPC and MSP1E3D1 containing GFP-rOCT1 mutants with amino acid exchanges in positions 160, 447 and 448. His-tagged GFP-rOCT1 mutants were reconstituted by cell free expression in the presence of empty NDs formed from POPC and His-tagged MSP1E3D1. The NDs were precipitated by Ni²⁺-NTA agarose beads and binding of 12.5 nM [³H]MPP⁺ was measured at 37°C in the presence of various concentrations of unlabeled MPP⁺. MPP⁺ binding was measured and numbers of transporter monomers were determined as in Figure 2B. Mean values ± S.D. of three experiments are indicated. A two-site binding model was fitted to the data. In the right panels, MPP⁺ binding and the fitted curves at low MPP⁺ concentrations are shown.

Fig. 6. Transport of MPP⁺ into proteoliposomes containing GFP-rOCT1 wildtype or mutants with amino acid exchanges in positions 218, 440 and 475. His-tagged GFP-rOCT1 (WT) or GFP-rOCT1 mutants were reconstituted into proteoliposomes formed with cholesterol, PC and PS. Uptake of 12.5 nM [³H]MPP⁺ into proteoliposomes was measured after 1 sec-incubation at 37°C in the presence of an outward-directed K⁺-diffusion potential and various concentrations of unlabeled MPP⁺. Nonspecific uptake measured in the presence of quinine was subtracted. Mean values ± S.D. of three experiments are indicated. The Michaelis Menten equation was fitted to the data. The apparent K_m values are indicated in parenthesis.

Fig. 7. Comparison between kinetic constants of GFP-rOCT1 wildtype and mutants with amino acid exchanges in positions 218, 440 and 475 determined for MPP⁺ uptake into proteoliposomes and for MPP⁺ binding to NDs formed with POPC. (A) Comparison between V_{max} values for MPP⁺ uptake and B_{max} values for MPP⁺ binding. (B) Comparison between apparent K_m values for MPP⁺ uptake and apparent K_D values for low-affinity MPP⁺ binding. The compiled data are presented in Figs. 3 and 6. The compared mean ± S.D. values were calculated from three individual experiments. The values are shown in Table 2. (*P<0.05, ***P<0.001) Significance of differences between V_{max} and B_{max} values and between apparent K_m and apparent K_D (low-aff.) values of individual mutants that were determined by two-way ANOVA using Bonferroni correction.

Fig. 8. Transport of MPP⁺ into proteoliposomes containing GFP-rOCT1 mutants with exchanges of amino acids in positions 160, 447 and 448 (A-D) and comparison between apparent K_m values for uptake and apparent K_D (low aff.) values for binding (E).

GFP-rOCT1 mutants were reconstituted into proteoliposomes formed with PC, PS and cholesterol. Uptake of 12.5 nM [^3H]MPP $^+$ into proteoliposomes was measured after 1 sec-incubation at 37°C in the presence of an outward-directed K $^+$ -diffusion potential and various concentrations of unlabeled MPP $^+$. (A-D) The Michaelis Menten equation was fitted to the compiled data sets. The curve obtained for the concentration dependence of MPP $^+$ uptake in proteoliposomes containing GFP-rOCT1 (WT) is indicated for comparison. The apparent K_m values (see Table 2) are indicated in parenthesis. (E) Comparison of apparent K_m values for MPP $^+$ uptake into proteoliposomes with apparent K_D values for low affinity MPP $^+$ binding to NDs formed with POPC. Mean values \pm S.D. from 3 experiments are indicated. Significance of difference between apparent K_m and apparent K_D (low aff.) values of individual mutants were determined by two-way ANOVA with Bonferroni correction (*** $P < 0.001$). For mutant GFP-rOCT1(L447Y) significance of a 2fold difference between apparent K_m and apparent K_D (low aff.) was not indicated by ANOVA but by Student's t-test ($P < 0.01$).

Fig. 9. Docking of MPP $^+$ to the modeled outward- and inward-open binding cleft of rOCT1. Docking was performed to previously built 3D homology models of rOCT1. Docking of MPP $^+$ molecules was restrained to occur within spheres of 7 Å around Trp218, Arg440 and Asp475. Thirty MPP $^+$ molecules with the highest docking energies for each transporter conformation were selected. 26 and 22 molecules were found to be located inside the outward- and inward-open cleft, respectively. Due to highly similar docking positions not all MPP $^+$ moieties are shown in the presentations.

TABLE 1

Binding of MPP⁺ to GFP-rOCT1 wildtype and GFP-rOCT1 mutants in nanodiscs formed with DMPG. Empty NDs were formed from DMPG and His-tagged MSP1E3D1. Fusion proteins between a non-dimerizing GFP mutant and rOCT1 wildtype, rOCT1(6ΔC) or single point mutants of rOCT1 were reconstituted into NDs by cell-free expression in the presence of the empty NDs. The NDs were bound to Ni²⁺-NTA-agarose beads and precipitated. Binding of MPP⁺ traced with [³H]MPP⁺ to the beads was measured at 37°C as described in Figure 2B. For individual experiments apparent K_D values and B_{max} values were determined by fitting a one-site binding model to the data. The amounts of GFP-fusion protein in the NDs were determined and B_{max} values per transporter monomer in the preparation were calculated. Means ± S.D. of three experiments are indicated. Significance of difference to GFP-rOCT1 was determined by one-way ANOVA with post-hoc Dunnett test (**P<0.01).

GFP-fusion proteins	app. K_D [μM]	B_{max} (MPP ⁺ /monomer)
GFP-rOCT1	31.7 ± 3.8	2.08 ± 0.07
GFP-rOCT1(6ΔC)	31.9 ± 3.4	2.10 ± 0.05
GFP-rOCT1(F160Y)	76.9 ± 6.5**	1.98 ± 0.06
GFP-rOCT1(W218Y)	15.6 ± 1.1	1.16 ± 0.11**
GFP-rOCT1(D475E)	24.1 ± 3.9	0.89 ± 0.07**
GFP-rOCT1(W218Y/D475E)	20.6 ± 1.2	1.11 ± 0.11**

TABLE 2

Comparison between MPP⁺ binding to GFP-rOCT1 wildtype and mutants in NDs with MPP⁺ uptake into proteoliposomes. NDs were prepared with POPC. The MPP⁺ binding measurements are shown in Figs. 3 and 5. B_{\max} (high aff.) and B_{\max} (low aff.) per rOCT1 monomer are indicated. Purified GFP-rOCT1 wildtype and mutants were reconstituted into proteoliposomes formed with cholesterol, PC and PS. The MPP⁺ uptake measurements are presented in Figs. 6 and 8. Means \pm S.D. of three experiments are shown. *P<0.05, **P<0.01 Significance of difference to GFP-rOCT1 determined by one-way ANOVA with post-hoc Dunnett test.

Fusionproteins	app. K_{D1} (high. aff.) [μ M]	app. K_{D2} (low aff.) [μ M]	B_{\max} (high aff.) MPP ⁺ per monomer	B_{\max} (low aff.) MPP ⁺ per monomer	app. K_m of MPP ⁺ uptake [μ M]	min. turnover of MPP ⁺ uptake per sec and monomer
GFP-rOCT1	0.23 \pm 0.02	36 \pm 2.6	0.93 \pm 0.05	2.29 \pm 0.05	19 \pm 3.1	17 \pm 2.1
GFP-rOCT1(6 Δ C)	0.25 \pm 0.01	39 \pm 5.8	1.04 \pm 0.04	2.10 \pm 0.04		
GFP-rOCT1(F160Y)	0.28 \pm 0.02	86 \pm 5.6**	1.07 \pm 0.04	2.04 \pm 0.05*	60 \pm 4.6**	20 \pm 3.0
GFP-rOCT1(W218Y)	0.34 \pm 0.05*	21 \pm 3.0	0.97 \pm 0.18	1.36 \pm 0.17**	15 \pm 1.0	9.6 \pm 1.3**
GFP-rOCT1(D475E)	0.21 \pm 0.04	28 \pm 4.7	0.81 \pm 0.06	1.29 \pm 0.06**	18 \pm 1.2	3.5 \pm 0.25**
GFP-rOCT1(W218Y/ D475E)	0.20 \pm 0.03	21 \pm 2.9	1.15 \pm 0.13	1.05 \pm 0.12**	20 \pm 3.4	3.7 \pm 0.38**
GFP-rOCT1(R440K)	0.30 \pm 0.06	81 \pm 15**	0.89 \pm 0.06	1.24 \pm 0.06**	69 \pm 4.5**	12 \pm 1.6**
GFP-rOCT1(R440K/ D475E)	0.32 \pm 0.06	n.d.	1.10 \pm 0.05	not detectable	26 \pm 4.7	0.73 \pm 0.15**
GFP-rOCT1(L447Y)	0.22 \pm 0.06	8.2 \pm 2.0**	0.81 \pm 0.20	2.08 \pm 0.20	8.6 \pm 0.3**	18 \pm 0.41
GFP-rOCT1(L447F)	0.26 \pm 0.02	14 \pm 1.6**	0.94 \pm 0.21	2.00 \pm 0.08*	8.7 \pm 0.4**	16 \pm 1.0
GFP-rOCT1(Q448E)	0.14 \pm 0.01	19 \pm 2.3*	0.92 \pm 0.19	2.19 \pm 0.18	13 \pm 0.9	19 \pm 1.9

Figures

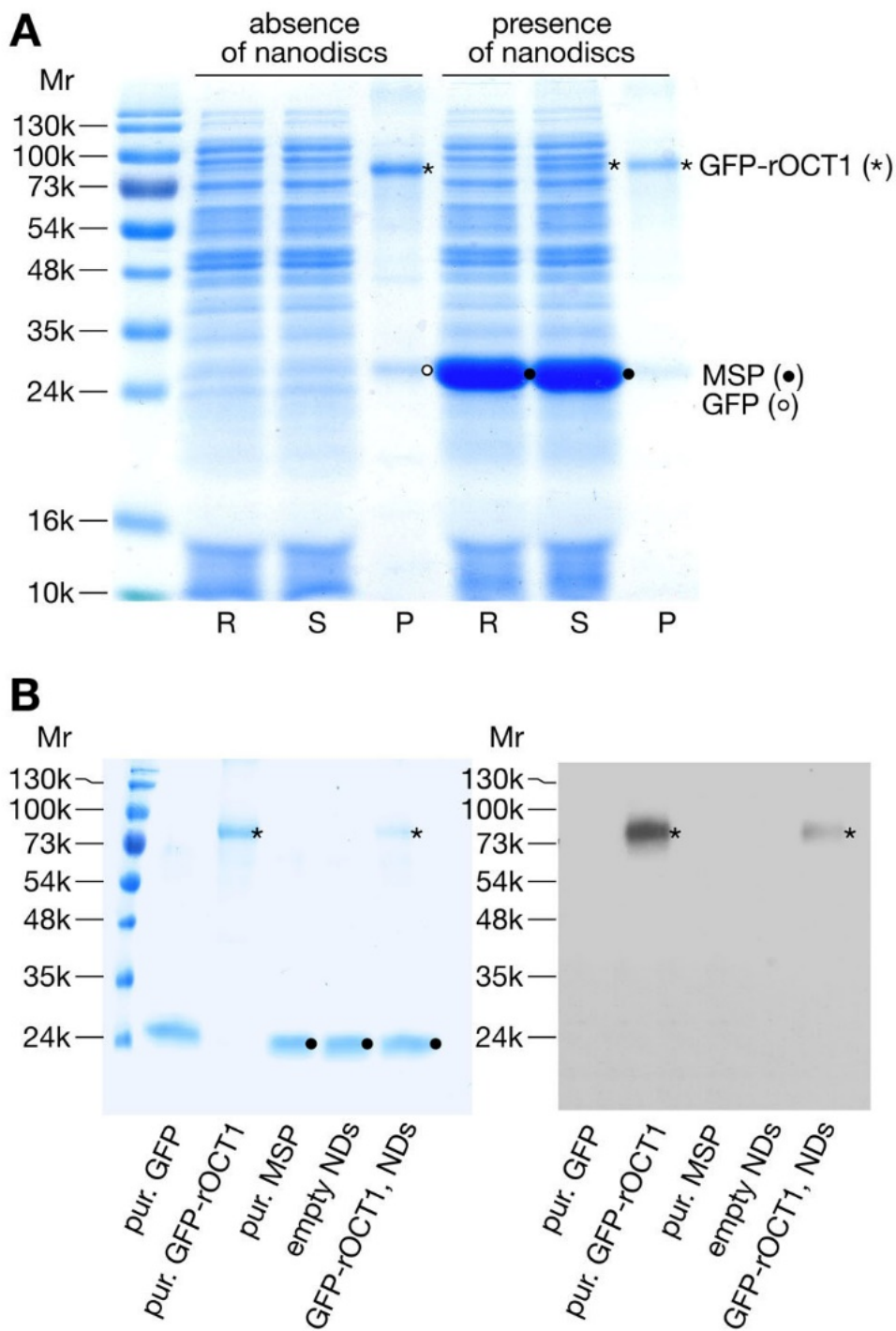


Fig. 1

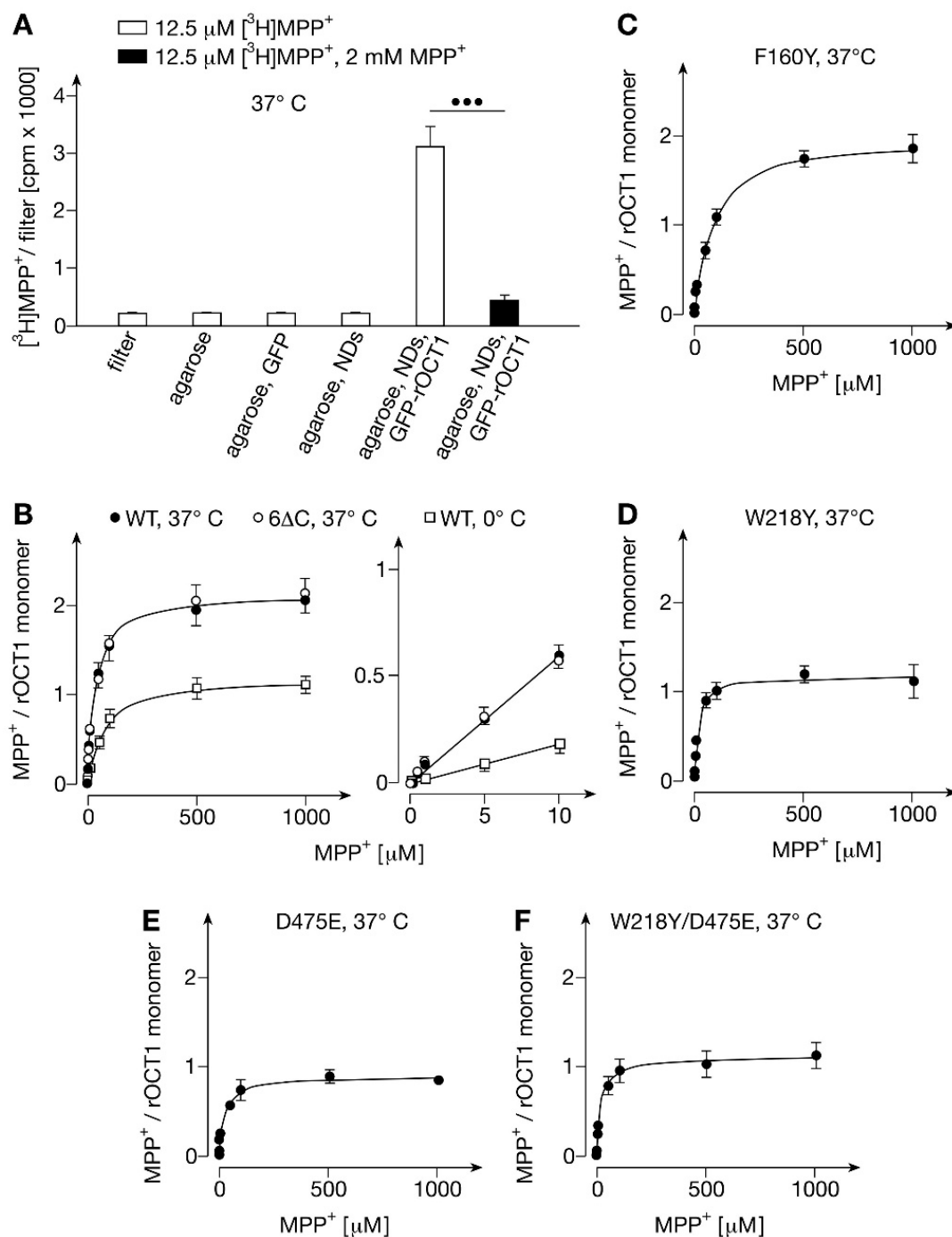


Fig. 2

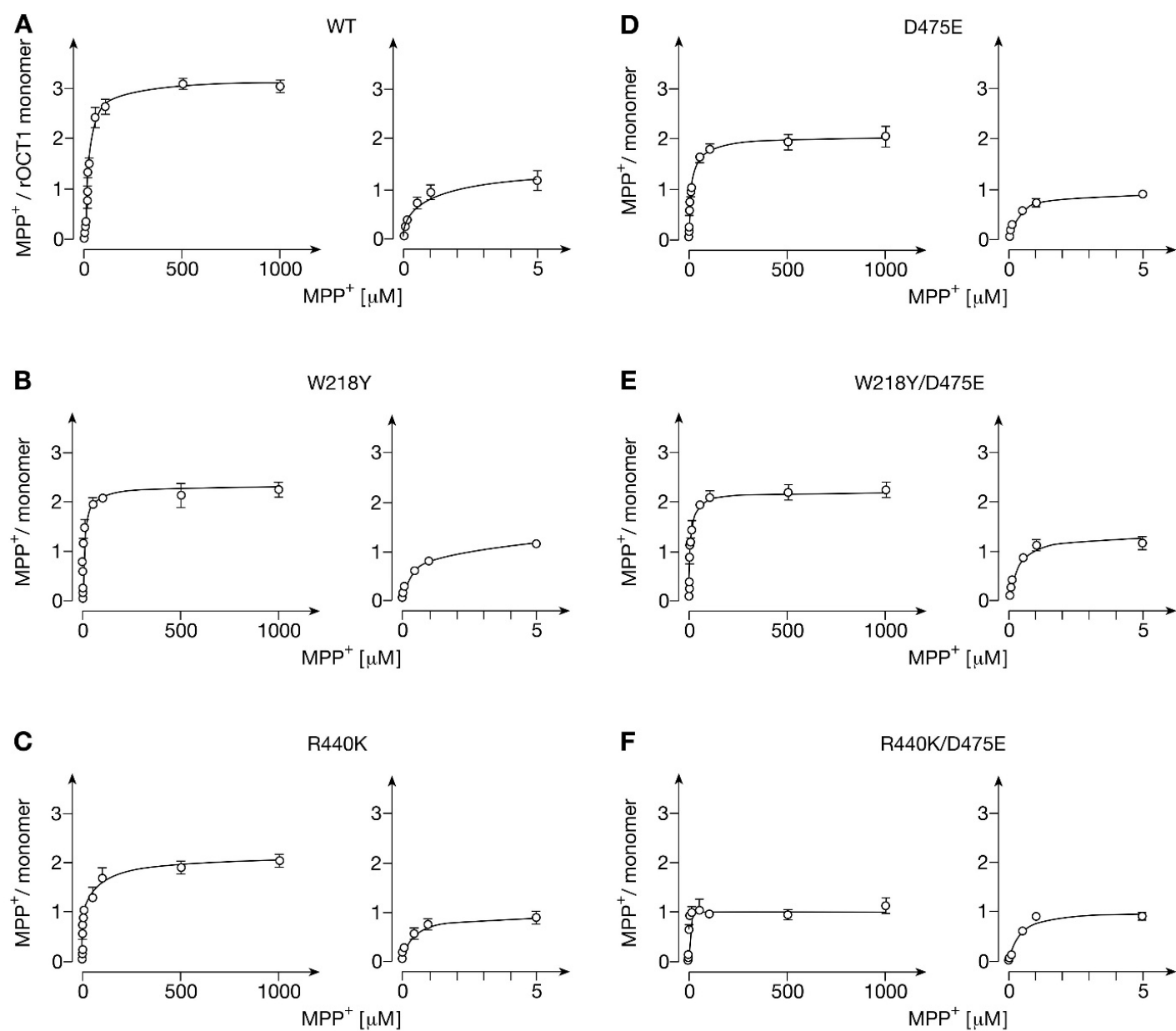


Fig. 3

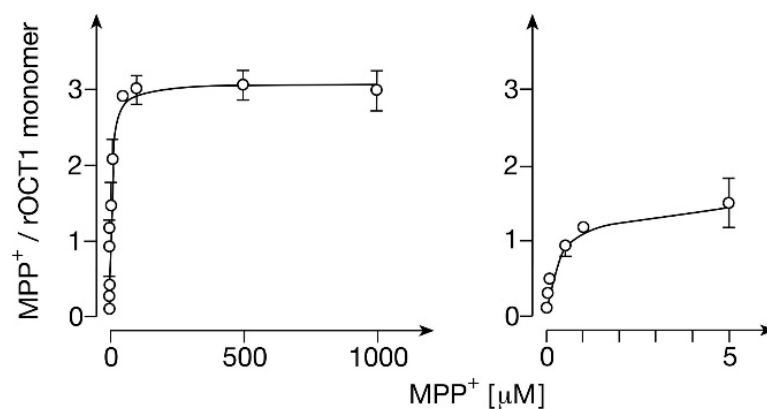


Fig. 4

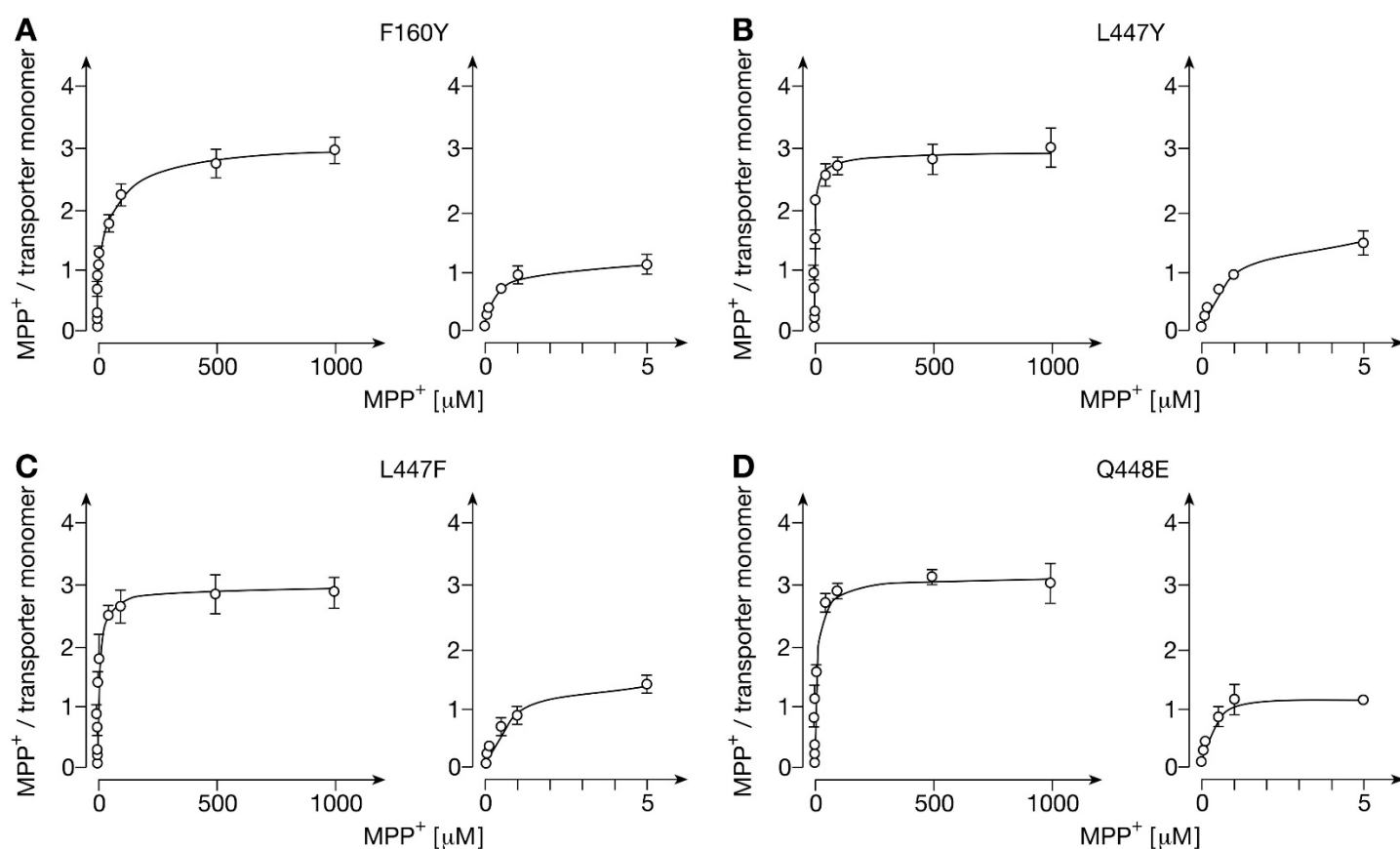


Fig. 5

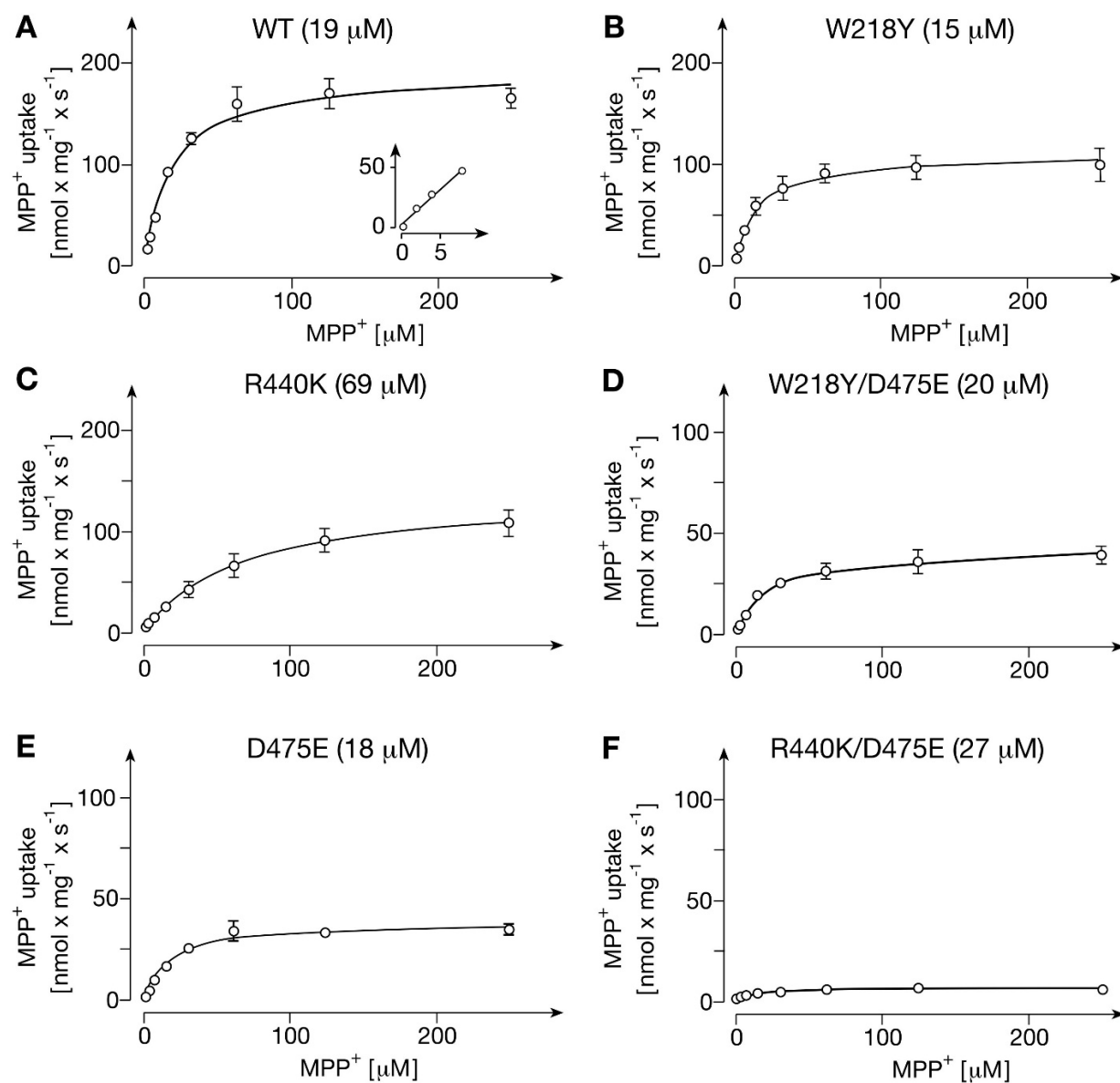


Fig. 6

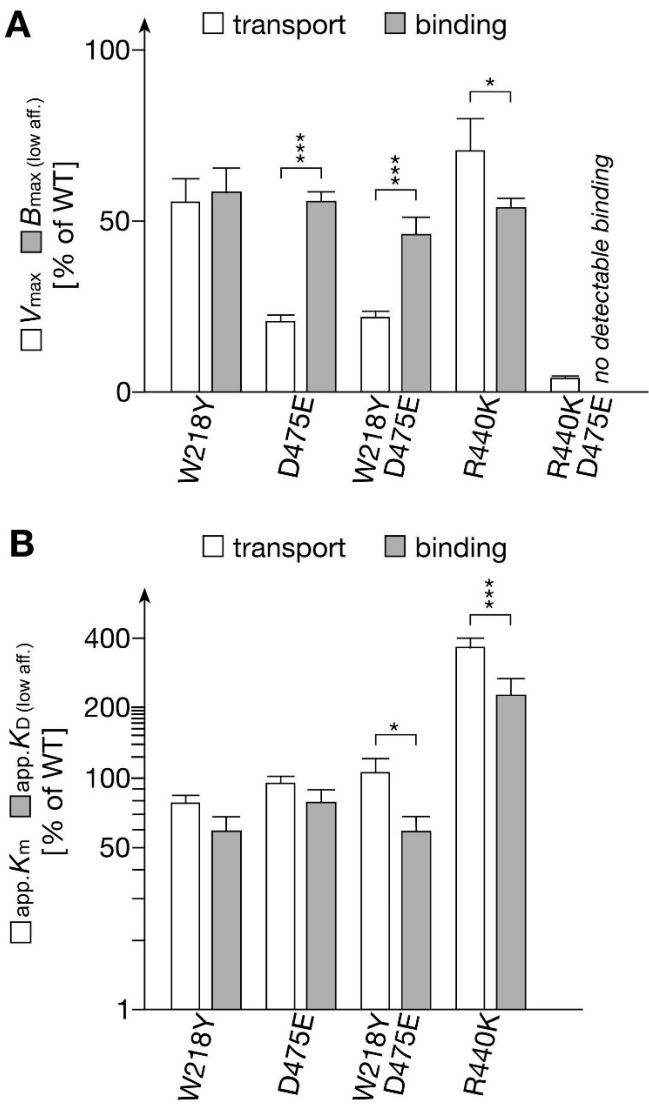


Fig. 7

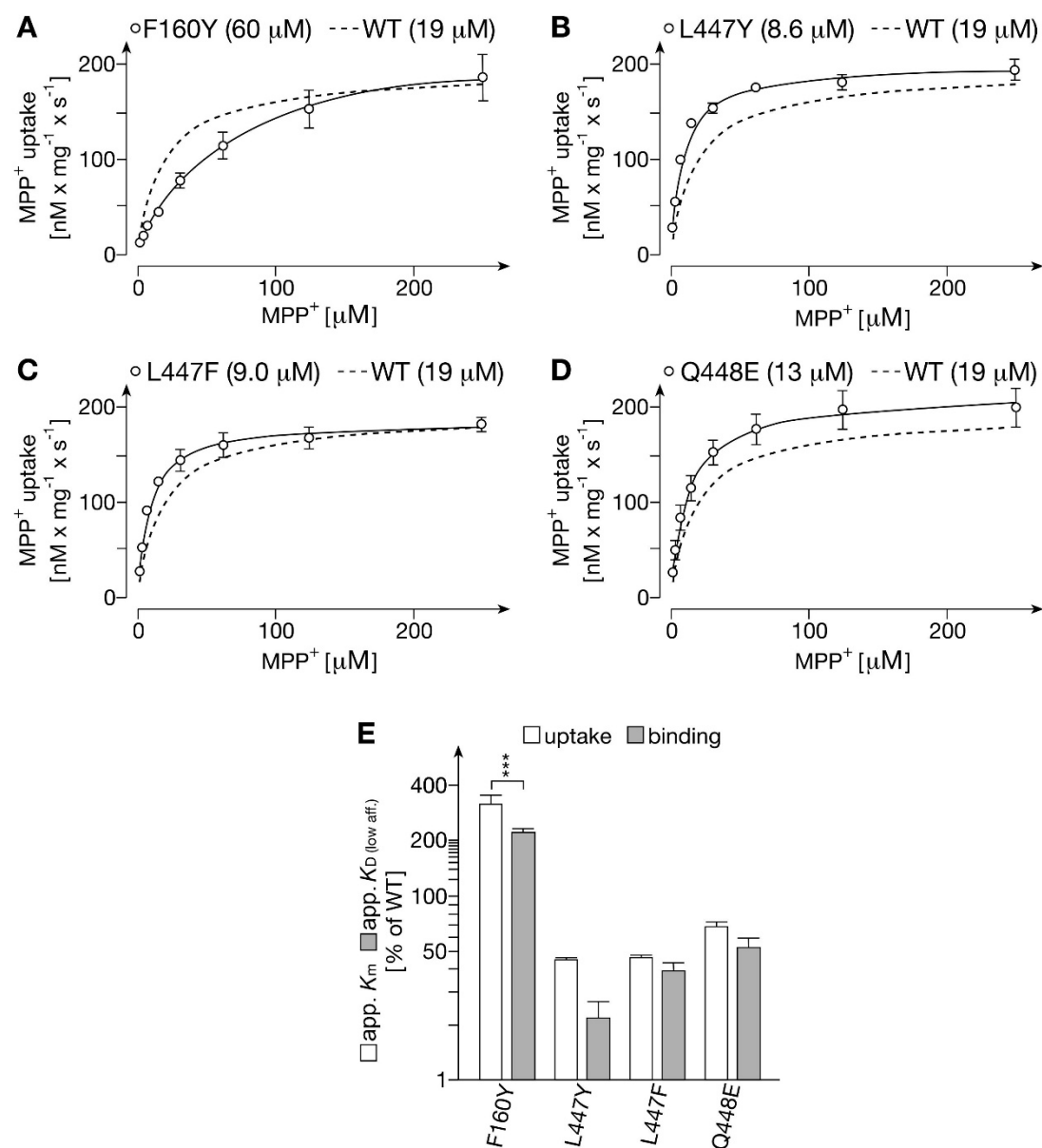


Fig. 8

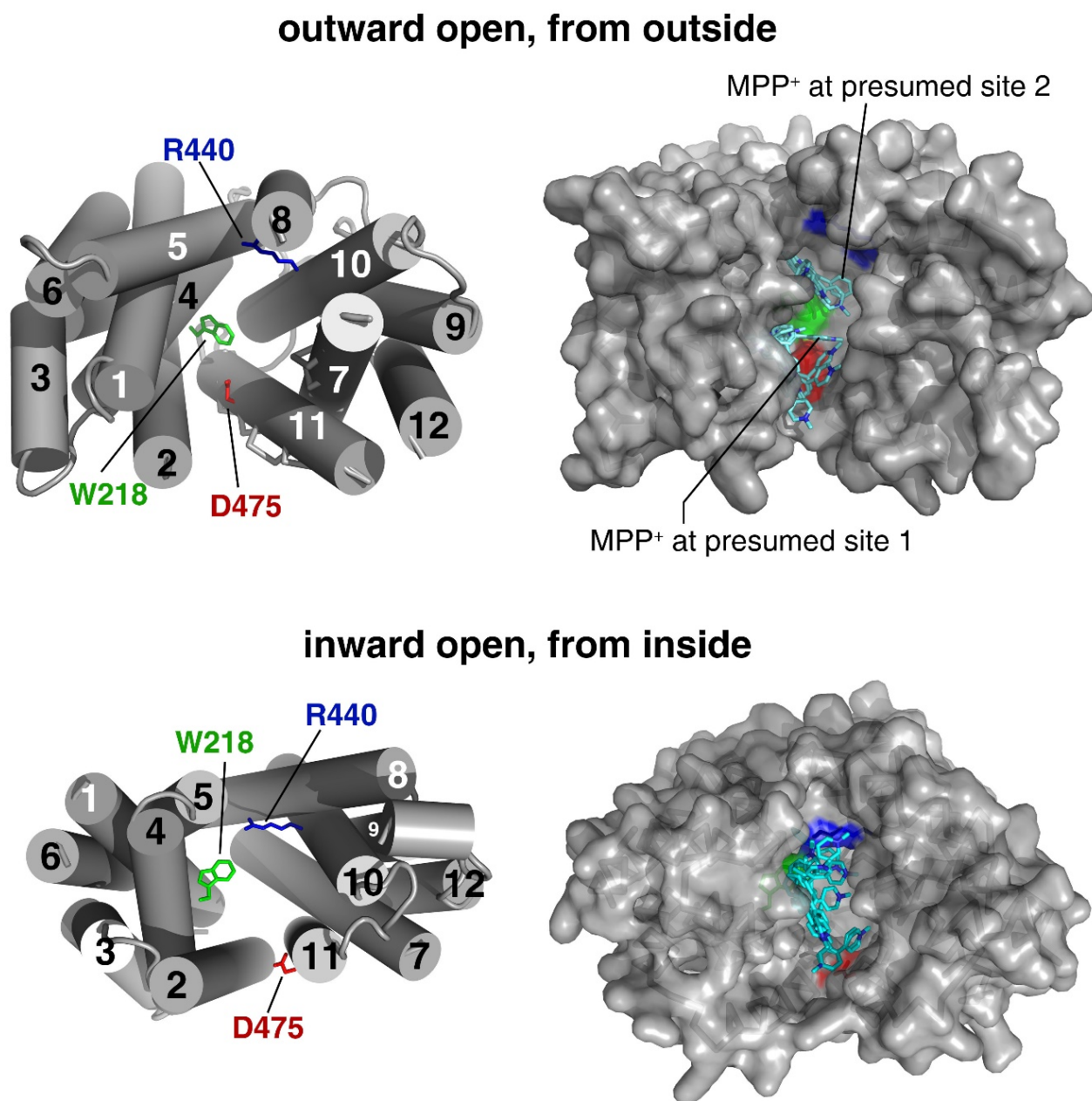


Fig. 9